

Effects of Structural Distortions on the Electronic Structure of T-type Transition Metal Dichalcogenides

Daniel T. Larson,¹ Wei Chen,^{1,2} Steven B. Torrisi,¹ Jennifer Coulter,³ Shiang Fang,^{1,4,*} and Efthimios Kaxiras^{1,3,†}

¹*Department of Physics, Harvard University, Cambridge, Massachusetts 02138, USA.*

²*Center for Functional Nanomaterials, Brookhaven National Laboratory, Upton, New York 11973, USA.*

³*John A. Paulson School of Engineering and Applied Sciences,
Harvard University, Cambridge, Massachusetts 02138, USA.*

⁴*Department of Physics and Astronomy, Center for Materials Theory, Rutgers University, Piscataway, NJ 08854 USA*

(Dated: January 14, 2022)

Single-layer transition metal dichalcogenides (TMDCs) can adopt two distinct structures corresponding to different coordination of the metal atoms. TMDCs adopting the T-type structure exhibit a rich and diverse set of phenomena, including charge density waves (CDW) in a $\sqrt{13} \times \sqrt{13}$ supercell pattern in TaS₂ and TaSe₂, and a possible excitonic insulating phase in TiSe₂. These properties make the T-TMDCs desirable components of layered heterostructure devices. In order to predict the emergent properties of combinations of different layered materials, one needs simple and accurate models for the constituent layers which can take into account potential effects of lattice mismatch, relaxation, strain, and structural distortion. Previous studies have developed *ab initio* tight-binding Hamiltonians for H-type TMDCs [1]. Here we extend this work to include T-type TMDCs. We demonstrate the capabilities of our model using three example systems: a 1-dimensional sinusoidal ripple, the 2×2 CDW in TiSe₂, and the $\sqrt{13} \times \sqrt{13}$ CDW in TaS₂. Using the technique of band unfolding we compare the electronic structure of the distorted crystals to the pristine band structure and find excellent agreement with direct DFT calculations, provided the magnitude of the distortions remains in the linear regime.

I. INTRODUCTION

There has been significant progress in the production of van der Waals heterostructures, devices formed by combinations of various two-dimensional layered materials [2]. These layers offer a promising platform for applications in optoelectronics [3], spintronics [4], valleytronics [5], straintronics [6, 7], twistrionics [8], nanomechanical resonators [9], and plasmonics [10]. Individual layers can be insulators, semimetals, or metals, and can express many different quantum orders, including charge density waves (CDW) [11], superconductivity (SC) [12], magnetism [13–15], topological phases [16, 17], and Mott insulator physics [18–21].

Transition metal dichalcogenides (TMDCs) are an interesting class of materials formed by a layer of transition metal atoms (M) sandwiched between layers of chalcogens (X) with the chemical formula MX₂, as shown in Figure 1. TMDCs built from group-VI transition metals, such as Mo and W, generally take on the H-structure in which the transition metal exhibits trigonal prismatic coordination by the chalcogens (point group D_{3h}), as shown in Figure 1(c)-(d). These materials, which are usually semiconductors, have become the subject of investigation for the past several years. TMDCs can also crystallize in the T-structure, in which the metal atom is octahedrally coordinated by the chalcogens (point group D_{3d}), as shown in Figure 1(a)-(b). For TMDCs containing group-IV or V transition metals, the T-structure is

typically metallic and either more stable or very close in energy to the H-phase. These T-type TMDCs, or T-TMDCs, are gaining attention because of their rich quantum phases. For example, with decreasing temperature, 1T-TaS₂ transitions from a high temperature normal metallic phase to an incommensurate CDW, near-commensurate CDW, and finally a commensurate CDW with Star-of-David clusters of Ta atoms with a $\sqrt{13} \times \sqrt{13}$ periodicity that gives rise to a correlated Mott insulator phase [22]. Under pressure, the Mott insulator phase melts and superconductivity develops around 2.5 GPa with T_c saturating at 5 K under high pressure [23]. In addition, there is a suggestion that TaS₂ should be considered a quantum spin liquid [20].

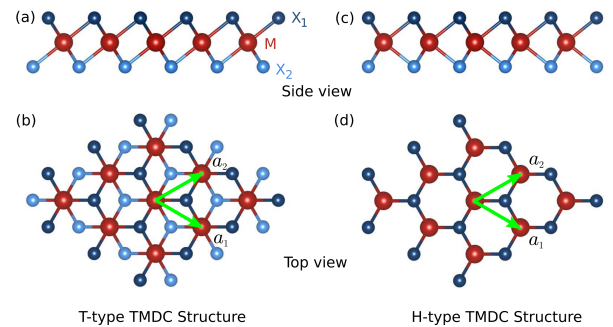


FIG. 1. T-type TMDC crystal structure seen from the side (a) and top (b). For comparison we show the H-type TMDC crystal in (c) and (d) from the side and top, respectively. \mathbf{a}_1 and \mathbf{a}_2 are the primitive lattice vectors of the 2D crystal (green arrows).

* shiangfang913@gmail.com

† kaxiras@physics.harvard.edu

In these T-type TMDCs, the existence of various elec-

tronic phases provides a platform to study their mutual competition and quantum criticality. Empirical tight-binding models have been constructed for the Ti based T-TMDCs [24] and for TaS₂ [25]. However, theoretical models for these T-type TMDCs are scarce compared to their H-type counterparts. In this work we provide comprehensive *ab initio* tight-binding Hamiltonians (TBH) for 9 different T-type TMDCs, considering the *d* orbitals from transition metal atoms and the *p* orbitals from the chalcogens. These Hamiltonians are extracted from the Wannier transformation of density functional theory (DFT) calculations without parameter fitting. In-plane strain is also included in the Hamiltonian modeling, capturing the coupling between electrons and long wavelength acoustic phonon modes. This provides a simple “parent” electronic band structure in which additional perturbations from CDW order or other deformations can be introduced, as long as the atomic displacements from the parent structure are not too large. The application of symmetry group analysis simplifies the modeling and elucidates the nature of the various coupling terms.

This paper is organized as follows: In Sec. II we survey some of the notable properties of the T-TMDC materials we have modeled. In Sec. III we provide details of the modeling procedure and give the explicit symmetry-constrained form of the tight-binding Hamiltonian that includes strain perturbations. Validation and analysis is provided in Sec. IV, followed by applications to three model systems in Sec. V, and finally our conclusions in Sec. VI. In the Appendix we tabulate the material-dependent numerical parameters extracted from DFT calculations for these tight-binding Hamiltonians.

II. T-TYPE TMDC MATERIAL PROPERTIES

Strain-dependent tight-binding models for group-VI TMDCs have been derived in previous work [1]. For these materials, specifically MX₂ with M = (Mo, W) and X = (S, Se), the H-structure is more stable than the T-structure, and most are semiconductors. In contrast, here we study group-IV and group-V TMDCs, with M = (Ti, Nb, Ta) and X = (S, Se, Te), where the H and T phases are very close in energy, as shown in Table I. The T-phase of the Ti compounds has a lower ground state energy than the H-phase, and for the group-V metals (Nb and Ta) the T-phase is within 100 meV of the H-phase. The values in Table I are the calculated energies of the materials in the undistorted T-structure, which have metallic band structures; examples are shown in Figure 2. The energies shown in Table I represent pristine unit cells in vacuum; in experimental contexts many factors, such as the presence of CDW distortions, substrates, finite temperature, chemical environment and intercalation, strain, and pressure, will affect the stability or metastability of a given phase [26–29]. The T-TMDCs we study are noteworthy for the diversity of CDW patterns which can both stabilize the structure and change

the electronic properties. Table I lists the various CDW patterns that have been observed in monolayer or bulk samples. Further, because the H-type to T-type transition can occur via a shift of a chalcogen layer, the kinetic barrier between the phases can be small enough for *in situ* manipulation; for instance, an STM tip was shown to reversibly control a transition between H- and T-type structures in NbSe₂ [30].

TABLE I. Summary of the single-layer T-type TMDCs considered, showing the calculated energy difference between single layers of the pristine T- and H-phases, $\Delta E = E_T - E_H$, in units of eV per formula unit (MX₂), and the lattice distortions that have been observed in the various T-phase crystals as multiples of the primitive unit cell, with references where these phases were observed. The last column contains the work function, $\Delta\Phi = E_{\text{vac}} - E_F$ (in eV), discussed later in Sec. III.D, for the relaxed, unstrained lattices.

Material	ΔE (eV)	T-structure CDW	$\Delta\Phi$ (eV)
TiS ₂	−0.43	—	5.64
TiSe ₂	−0.36	2×2 [31]	5.22
TiTe ₂	−0.31	2×2 [32]	4.70
NbS ₂	0.10	—	5.20
NbSe ₂	0.09	$\sqrt{13} \times \sqrt{13}$ [18]	4.80
NbTe ₂	0.00	3×1 [33]	4.51
TaS ₂	0.07	$\sqrt{13} \times \sqrt{13}$ [34]	4.95
TaSe ₂	0.07	$\sqrt{13} \times \sqrt{13}$ [35]	4.57
TaTe ₂	0.00	3×1, 3×3 [36]	4.32

Because of these diverse CDW orders and the interplay with superconductivity, group-IV and V TMDCs have been the subject of much recent research. In the following we provide a brief summary of the most interesting features of each of type of material as motivation for the strain-dependent electronic structure modeling described in the next section. More comprehensive reviews and additional references can be found in [37–39].

TiSe₂ is intriguing because it exhibits a 2 × 2 CDW, a possible excitonic insulating phase [40], and, with doping to suppress the CDW state, superconductivity [41, 42]. As a result, the CDW phase has been the subject of study in relation to electronic, excitonic, and vibrational structure effects, and much ongoing investigation focuses on the nature of the CDW transition [43–45]. Single-layer TiTe₂ also exhibits a 2 × 2 CDW, but it is not observed in samples with 2 or more layers [32]. Previous theoretical work has shown that single-layer TiS₂ is a semimetal with increasing band overlap under compressive strain, but switches to a semiconductor with a gap that grows with tensile strain [46].

NbS₂ and NbSe₂ have proven to be challenging to produce in the 1T-structure. There is a single report of experimental production of the 1T polytype of NbS₂ using atmospheric pressure chemical vapor deposition [47]. Recently, Nakata *et al.* [18] have successfully grown single-layer NbSe₂ on bilayer graphene and shown that the phase, T *vs* H, can be controlled by the substrate temperature during growth. It has also been demonstrated

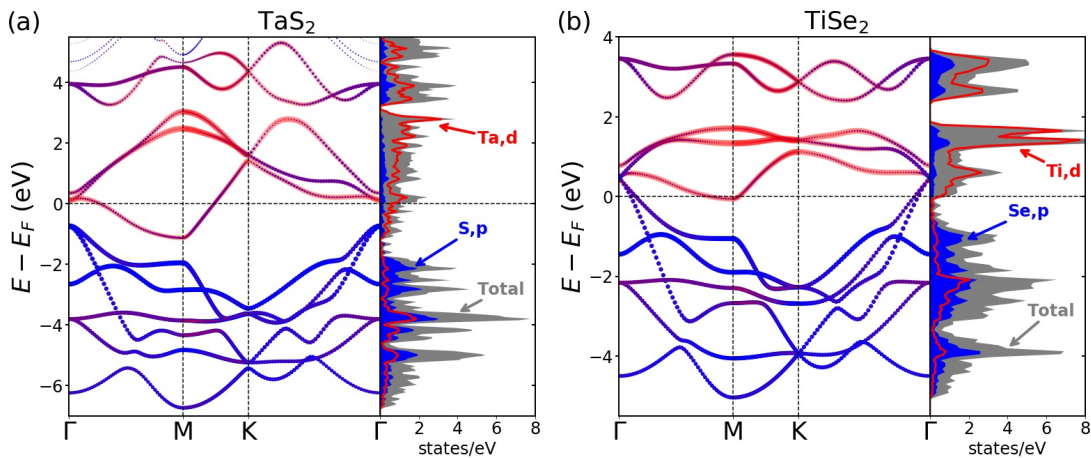


FIG. 2. DFT band structure and density of states (DOS) for two T-type TMDCs: (a) TaS₂ and (b) TiSe₂, showing the 11 bands nearest the Fermi level. The valence band character is dominated by the chalcogen *p*-orbitals, while the transition metal *d*-orbitals dominate the conduction band character. A notable feature is the large peak in the conduction band DOS for TiSe₂ which is absent for TaS₂.

that the interaction between an STM tip and the sample can induce a reversible 2H to 1T phase transition in NbSe₂ [30]. On the other hand, bulk NbTe₂ takes on the 1T-structure but with a significant 3×1 CDW distortion [33], and also exhibits superconductivity at temperatures below 1 K [48]. The niobium-based TMDCs are d^1 materials, so the simplest ionic picture would predict metallic behavior with a single half-filled band crossing the Fermi surface. However, ARPES measurements on NbSe₂ [18] and NbTe₂ [33] do not show any quasiparticle crossings.

The tantalum-based TMDCs are perhaps best known for their rich CDW phases competing with superconductivity. TaS₂ and TaSe₂ are formally d^1 materials and are indeed metallic at high temperatures, but as the temperature is lowered they develop incommensurate, nearly-commensurate, and finally a commensurate $\sqrt{13} \times \sqrt{13}$ CDW phase. This latter phase is a correlated Mott insulator [22]. When the CDW phase is suppressed by either chemical doping, applying high pressure, or chalcogen substitution, superconductivity can arise at temperatures of a few K [23, 49–51]. On the other hand, TaTe₂ exhibits similar behavior to NbTe₂ at room temperature, including a 3×1 CDW reconstruction, but at temperatures below ~ 170 K it displays a competing 3×3 CDW [36] and no superconductivity [33].

III. TIGHT-BINDING HAMILTONIAN FOR THE MONOLAYER WITH STRAIN

A. Numerical Methods

DFT calculations were performed using the VASP code [52, 53] with the PBE exchange-correlation functional [54]. Projector augmented wave (PAW) pseu-

dopotentials included 6 valence electrons (s^2p^4) for the chalcogens and 11, 12, and 13 valence electrons for Ta ($5p^66s^15d^4$), Ti ($3s^23p^64s^13d^3$), and Nb ($4s^24p^65s^14d^4$), respectively. A plane-wave energy cutoff of 420 eV was used for all materials, along with van der Waals corrections using the zero-damping DFT-D3 method [55]. We employed a Γ -centered $25 \times 25 \times 1$ k-point grid. All structural relaxations were carried out until the Hellman-Feynman forces on each atom had a magnitude below 0.001 eV/Å. The maximally localized Wannier transformations were performed using the Wannier90 code [56].

B. General Formulation of Strained Crystal Lattices

As viewed from above in Fig. 1 (b), the TMDCs T-structure consists of 3 interpenetrating triangular lattices. Seen from the side, the transition metal lattice is sandwiched between chalcogen lattices above and below, in such a way that the metal atom is octahedrally coordinated. To model a monolayer T-TMDC we choose the primitive lattice vectors to be $\mathbf{a}_1 = \frac{\sqrt{3}}{2}a\hat{x} - \frac{1}{2}a\hat{y}$ and $\mathbf{a}_2 = \frac{\sqrt{3}}{2}a\hat{x} + \frac{1}{2}a\hat{y}$. The metal atom is located at the origin and the horizontal position of the upper (lower) chalcogen atom is taken to be $\pm(\mathbf{a}_1 + \mathbf{a}_2)/3$.

Effects of in-plane strain on the electronic structure can be studied in the same way as they were for H-type TMDCs [1], namely by displacing the crystal coordinates according to a vector field $\mathbf{u} = (u_x(x, y), u_y(x, y))$, where $\mathbf{r} = (x, y)$ gives the coordinates in the unstrained crystal and the location in the strained crystal is given by $\mathbf{r} + \mathbf{u}$. Since no physical change arises from a constant displacement, the strain field is characterized by the symmetrized

derivative of \mathbf{u} and written:

$$u_{ij} = \frac{1}{2} (\partial_i u_j + \partial_j u_i)$$

with $i, j = x, y$. Under the C_{3v} symmetry group of the crystal the strain field can be decomposed into a scalar part, $u_{xx} + u_{yy}$, representing biaxial isotropic strain, and a doublet, $(u_{xx} - u_{yy}, -2u_{xy})$, representing anisotropic strain and shear. The antisymmetrized derivative $\omega_{xy} = \frac{1}{2} (\partial_x u_y - \partial_y u_x)$ is also a scalar under rotations and represents a local rotation of the coordinates by an angle ω_{xy} .

By calculating the electronic structure of the crystal subjected to different amounts of uniform strain ($u_{ij} = \text{constant}$), we can then approximate the response to a slowly varying strain field by assuming a constant strain over any small region, referred to as a “local strain approximation”. In this manner we can study the interaction between the electronic structure and long-wavelength acoustic phonons.

The first step, considering only the physical structure, is to use DFT to optimize the lattice constant for the unstrained crystal. From the optimized crystal we can determine the height, h , of the chalcogen atoms above (and below) the plane of the metal atoms by relaxing the internal coordinates of a cell where the components of the lattice vectors, \mathbf{a}_i for $i = 1, 2, 3$, have been modified by the constant strain field as follows:

$$a'_{ix} = a_{ix} + u_{xx}a_{ix} + u_{yx}a_{iy} \quad (1)$$

$$a'_{iy} = a_{iy} + u_{xy}a_{ix} + u_{yy}a_{iy} \quad (2)$$

$$a'_{iz} = a_{iz}. \quad (3)$$

As a function of the isotropic strain, the height h of the chalcogens above and below the metal layer can be parametrized as

$$h = d_0 - d_1(u_{xx} + u_{yy}). \quad (4)$$

Our results for the lattice constants, a , unstrained chalcogen distances, d_0 , and coefficient d_1 , are given in Table II. Several general trends are readily apparent in the results, in particular the increase in both lattice constant and chalcogen height with the atomic number of the chalcogen.

C. Tight-Binding Hamiltonian with Strain

Having obtained the structural parameters for each material under study, we use DFT calculations of the

electronic structure followed by a transformation to an atomic-like basis of maximally localized Wannier functions (MLWF) [57, 58] in order to determine the tight-binding parameters for a range of input strain values. By fitting the variations in the parameters as a function of u_{xx} , u_{yy} , and u_{xy} we arrive at a complete tight-binding Hamiltonian for any choice of uniform strain.

TABLE II. Calculated equilibrium lattice constant, a (Å), distance of the chalcogen from the basal plane in the unstrained crystal, d_0 (Å), and coefficient d_1 (Å) from Eq. (4), representing the response of the chalcogen height to isotropic strain for the TMDC MX₂.

M \ X	S	Se	Te	
Ti	a	3.41	3.53	3.74
	d_0	1.42	1.56	1.75
	d_1	0.71	0.76	0.83
Nb	a	3.35	3.46	3.62
	d_0	1.55	1.68	1.87
	d_1	0.70	0.78	0.80
Ta	a	3.36	3.49	3.64
	d_0	1.54	1.66	1.85
	d_1	0.70	0.75	0.86

A monolayer T-type TMDC has D_{3d} symmetry, which includes xz mirror symmetry, C_2 rotation symmetry about the y -axis, inversion symmetry, and \mathcal{R}_3 rotation symmetry about the z -axis. The 3-fold rotational symmetry of the crystal means that hopping terms to equivalent neighbor atoms will appear differently in a Hamiltonian matrix with a fixed rectangular coordinate system. However, careful choice of reference hopping vectors and analysis of the symmetry-allowed matrix elements results in significant constraints on the form of the Hamiltonian matrix.

Our model of the electronic band structure includes 11 orbitals: five d -orbitals, d_{xy} , d_{yz} , $d_{x^2-y^2}$, d_{xz} , and d_{z^2} from the metal atom at the M site (origin), and three p -orbitals, p_x , p_y , and p_z from each chalcogen atom, located at X₁ (upper) and X₂ (lower) sites. In what follows we use this ordering of basis orbitals to define the tight-binding Hamiltonian, including hopping terms up to 3rd nearest neighbor (3NN) and all dependence on isotropic and anisotropic strain, $(u_{xx} + u_{yy})$ and $(u_{xx} - u_{yy}, 2u_{xy})$, respectively.

The on-site energy represents the interactions between orbitals located at the same atom. At X₁ sites the chalcogen p -orbital on-site energy has the form:

$$H = \begin{bmatrix} \epsilon_0 & 0 & 0 \\ 0 & \epsilon_0 & 0 \\ 0 & 0 & \epsilon_1 \end{bmatrix} + (u_{xx} + u_{yy}) \begin{bmatrix} \alpha_0^{(0)} & 0 & 0 \\ 0 & \alpha_0^{(0)} & 0 \\ 0 & 0 & \alpha_1^{(0)} \end{bmatrix} + (u_{xx} - u_{yy}) \begin{bmatrix} \beta_0^{(0)} & 0 & \beta_1^{(0)} \\ 0 & -\beta_0^{(0)} & 0 \\ \beta_1^{(0)} & 0 & 0 \end{bmatrix} + (2u_{xy}) \begin{bmatrix} 0 & \beta_0^{(0)} & 0 \\ \beta_0^{(0)} & 0 & -\beta_1^{(0)} \\ 0 & -\beta_1^{(0)} & 0 \end{bmatrix} \quad (5)$$

At X₂ sites, the on-site Hamiltonian is the same as the ones at X₁ sites (including strain). At M sites the metal

d -orbital on-site Hamiltonian reads:

$$\begin{aligned}
H = & \begin{bmatrix} \epsilon_2 & \epsilon_5 & 0 & 0 & 0 \\ \epsilon_5 & \epsilon_3 & 0 & 0 & 0 \\ 0 & 0 & \epsilon_2 & -\epsilon_5 & 0 \\ 0 & 0 & -\epsilon_5 & \epsilon_3 & 0 \\ 0 & 0 & 0 & 0 & \epsilon_4 \end{bmatrix} + (u_{xx} + u_{yy}) \begin{bmatrix} \alpha_2^{(0)} & \alpha_5^{(0)} & 0 & 0 & 0 \\ \alpha_5^{(0)} & \alpha_3^{(0)} & 0 & 0 & 0 \\ 0 & 0 & \alpha_2^{(0)} & -\alpha_5^{(0)} & 0 \\ 0 & 0 & -\alpha_5^{(0)} & \alpha_3^{(0)} & 0 \\ 0 & 0 & 0 & 0 & \alpha_4^{(0)} \end{bmatrix} \\
& + (u_{xx} - u_{yy}) \begin{bmatrix} \beta_2^{(0)} & \beta_4^{(0)} & 0 & 0 & 0 \\ \beta_4^{(0)} & \beta_3^{(0)} & 0 & 0 & 0 \\ 0 & 0 & -\beta_2^{(0)} & \beta_4^{(0)} & \beta_5^{(0)} \\ 0 & 0 & \beta_4^{(0)} & -\beta_3^{(0)} & \beta_6^{(0)} \\ 0 & 0 & \beta_5^{(0)} & \beta_6^{(0)} & 0 \end{bmatrix} + (2u_{xy}) \begin{bmatrix} 0 & 0 & \beta_2^{(0)} & -\beta_4^{(0)} & \beta_5^{(0)} \\ 0 & 0 & \beta_4^{(0)} & -\beta_3^{(0)} & -\beta_6^{(0)} \\ \beta_2^{(0)} & \beta_4^{(0)} & 0 & 0 & 0 \\ -\beta_4^{(0)} & -\beta_3^{(0)} & 0 & 0 & 0 \\ \beta_5^{(0)} & -\beta_6^{(0)} & 0 & 0 & 0 \end{bmatrix}
\end{aligned} \tag{6}$$

Each atom has 6 nearest neighbors (1NN), 3 from each of the other two sites. There are three types of first-neighbor interactions: (X₁-M), (X₂-M) and (X₂-X₁). For the (X₁-M) interaction we take as a reference bond the hopping from M at the origin to X₁ at $(\mathbf{a}_1 + \mathbf{a}_2)/3$. The corresponding Hamiltonian is:

$$\begin{aligned}
H = & \begin{bmatrix} 0 & 0 & t_0^{(1)} & t_1^{(1)} & t_2^{(1)} \\ t_3^{(1)} & t_4^{(1)} & 0 & 0 & 0 \\ 0 & 0 & t_5^{(1)} & t_6^{(1)} & t_7^{(1)} \end{bmatrix} + (u_{xx} + u_{yy}) \begin{bmatrix} 0 & 0 & \alpha_0^{(1)} & \alpha_1^{(1)} & \alpha_2^{(1)} \\ \alpha_3^{(1)} & \alpha_4^{(1)} & 0 & 0 & 0 \\ 0 & 0 & \alpha_5^{(1)} & \alpha_6^{(1)} & \alpha_7^{(1)} \end{bmatrix} \\
& + (u_{xx} - u_{yy}) \begin{bmatrix} 0 & 0 & \beta_0^{(1)} & \beta_1^{(1)} & \beta_2^{(1)} \\ \beta_3^{(1)} & \beta_4^{(1)} & 0 & 0 & 0 \\ 0 & 0 & \beta_5^{(1)} & \beta_6^{(1)} & \beta_7^{(1)} \end{bmatrix} + (2u_{xy}) \begin{bmatrix} \beta_8^{(1)} & \beta_9^{(1)} & 0 & 0 & 0 \\ 0 & 0 & \beta_{10}^{(1)} & \beta_{11}^{(1)} & \beta_{12}^{(1)} \\ \beta_{13}^{(1)} & \beta_{14}^{(1)} & 0 & 0 & 0 \end{bmatrix}
\end{aligned} \tag{7}$$

For the (X₂-M) interaction, with the hopping from M at the origin to X₂ at $-(\mathbf{a}_1 + \mathbf{a}_2)/3$ taken as the reference, the Hamiltonian has the same form as (X₁-M) with an overall (-1) factor. The final first neighbor coupling, (X₂-X₁), with reference bond chosen along the positive x -axis, has the form:

$$\begin{aligned}
H = & \begin{bmatrix} t_8^{(1)} & 0 & t_{11}^{(1)} \\ 0 & t_9^{(1)} & 0 \\ t_{11}^{(1)} & 0 & t_{10}^{(1)} \end{bmatrix} + (u_{xx} + u_{yy}) \begin{bmatrix} \alpha_8^{(1)} & 0 & \alpha_{11}^{(1)} \\ 0 & \alpha_9^{(1)} & 0 \\ \alpha_{11}^{(1)} & 0 & \alpha_{10}^{(1)} \end{bmatrix} \\
& + (u_{xx} - u_{yy}) \begin{bmatrix} \beta_{15}^{(1)} & 0 & \beta_{18}^{(1)} \\ 0 & \beta_{16}^{(1)} & 0 \\ \beta_{18}^{(1)} & 0 & \beta_{17}^{(1)} \end{bmatrix} + (2u_{xy}) \begin{bmatrix} 0 & \beta_{19}^{(1)} & 0 \\ \beta_{19}^{(1)} & 0 & \beta_{20}^{(1)} \\ 0 & \beta_{20}^{(1)} & 0 \end{bmatrix}
\end{aligned} \tag{8}$$

Each atom has 6 second neighbors (2NN) of the same type. In each case the reference bond is along the positive y -axis. The (X₁-X₁) coupling has the form:

$$\begin{aligned}
H = & \begin{bmatrix} t_0^{(2)} & t_3^{(2)} & t_4^{(2)} \\ -t_3^{(2)} & t_1^{(2)} & t_5^{(2)} \\ t_4^{(2)} & -t_5^{(2)} & t_2^{(2)} \end{bmatrix} + (u_{xx} + u_{yy}) \begin{bmatrix} \alpha_0^{(2)} & \alpha_3^{(2)} & \alpha_4^{(2)} \\ -\alpha_3^{(2)} & \alpha_1^{(2)} & \alpha_5^{(2)} \\ \alpha_4^{(2)} & -\alpha_5^{(2)} & \alpha_2^{(2)} \end{bmatrix} \\
& + (u_{xx} - u_{yy}) \begin{bmatrix} \beta_0^{(2)} & \beta_3^{(2)} & \beta_4^{(2)} \\ -\beta_3^{(2)} & \beta_1^{(2)} & \beta_5^{(2)} \\ \beta_4^{(2)} & -\beta_5^{(2)} & \beta_2^{(2)} \end{bmatrix} + (2u_{xy}) \begin{bmatrix} 0 & \beta_6^{(2)} & \beta_7^{(2)} \\ \beta_6^{(2)} & 0 & \beta_8^{(2)} \\ -\beta_7^{(2)} & \beta_8^{(2)} & 0 \end{bmatrix}
\end{aligned} \tag{9}$$

while the (X₂-X₂) interaction has some (-1) phase factors compared to (X₁-X₁), as shown:

$$\begin{aligned}
H = & \begin{bmatrix} t_0^{(2)} & -t_3^{(2)} & t_4^{(2)} \\ t_3^{(2)} & t_1^{(2)} & -t_5^{(2)} \\ t_4^{(2)} & t_5^{(2)} & t_2^{(2)} \end{bmatrix} + (u_{xx} + u_{yy}) \begin{bmatrix} \alpha_0^{(2)} & -\alpha_3^{(2)} & \alpha_4^{(2)} \\ \alpha_3^{(2)} & \alpha_1^{(2)} & -\alpha_5^{(2)} \\ \alpha_4^{(2)} & \alpha_5^{(2)} & \alpha_2^{(2)} \end{bmatrix} \\
& + (u_{xx} - u_{yy}) \begin{bmatrix} \beta_0^{(2)} & -\beta_3^{(2)} & \beta_4^{(2)} \\ \beta_3^{(2)} & \beta_1^{(2)} & -\beta_5^{(2)} \\ \beta_4^{(2)} & \beta_5^{(2)} & \beta_2^{(2)} \end{bmatrix} + (2u_{xy}) \begin{bmatrix} 0 & \beta_6^{(2)} & -\beta_7^{(2)} \\ \beta_6^{(2)} & 0 & \beta_8^{(2)} \\ \beta_7^{(2)} & \beta_8^{(2)} & 0 \end{bmatrix}
\end{aligned} \tag{10}$$

The Hamiltonian for the (M-M) interaction has the form:

$$\begin{aligned}
 H = & \begin{bmatrix} t_6^{(2)} & t_{11}^{(2)} & 0 & 0 & 0 \\ t_{11}^{(2)} & t_7^{(2)} & 0 & 0 & 0 \\ 0 & 0 & t_8^{(2)} & t_{12}^{(2)} & t_{13}^{(2)} \\ 0 & 0 & t_{12}^{(2)} & t_9^{(2)} & t_{14}^{(2)} \\ 0 & 0 & t_{13}^{(2)} & t_{14}^{(2)} & t_{10}^{(2)} \end{bmatrix} + (u_{xx} + u_{yy}) \begin{bmatrix} \alpha_6^{(2)} & \alpha_{11}^{(2)} & 0 & 0 & 0 \\ \alpha_{11}^{(2)} & \alpha_7^{(2)} & 0 & 0 & 0 \\ 0 & 0 & \alpha_8^{(2)} & \alpha_{12}^{(2)} & \alpha_{13}^{(2)} \\ 0 & 0 & \alpha_{12}^{(2)} & \alpha_9^{(2)} & \alpha_{14}^{(2)} \\ 0 & 0 & \alpha_{13}^{(2)} & \alpha_{14}^{(2)} & \alpha_{10}^{(2)} \end{bmatrix} \\
 & + (u_{xx} - u_{yy}) \begin{bmatrix} \beta_9^{(2)} & \beta_{14}^{(2)} & 0 & 0 & 0 \\ \beta_{14}^{(2)} & \beta_{10}^{(2)} & 0 & 0 & 0 \\ 0 & 0 & \beta_{11}^{(2)} & \beta_{15}^{(2)} & \beta_{16}^{(2)} \\ 0 & 0 & \beta_{15}^{(2)} & \beta_{12}^{(2)} & \beta_{17}^{(2)} \\ 0 & 0 & \beta_{16}^{(2)} & \beta_{17}^{(2)} & \beta_{13}^{(2)} \end{bmatrix} + (2u_{xy}) \begin{bmatrix} 0 & 0 & \beta_{18}^{(2)} & \beta_{19}^{(2)} & \beta_{20}^{(2)} \\ 0 & 0 & \beta_{21}^{(2)} & \beta_{22}^{(2)} & \beta_{23}^{(2)} \\ \beta_{18}^{(2)} & \beta_{21}^{(2)} & 0 & 0 & 0 \\ \beta_{19}^{(2)} & \beta_{22}^{(2)} & 0 & 0 & 0 \\ \beta_{20}^{(2)} & \beta_{23}^{(2)} & 0 & 0 & 0 \end{bmatrix}
 \end{aligned} \tag{11}$$

Similar to first neighbor coupling, each atom has 3 third neighbors (3NN) of each of the other two types, but with different reference bonds. The (X₁-M) interaction, with reference bond pointing from the origin to $-2(\mathbf{a}_1 + \mathbf{a}_2)/3$, takes the form:

$$\begin{aligned}
 H = & \begin{bmatrix} 0 & 0 & t_0^{(3)} & t_1^{(3)} & t_2^{(3)} \\ t_3^{(3)} & t_4^{(3)} & 0 & 0 & 0 \\ 0 & 0 & t_5^{(3)} & t_6^{(3)} & t_7^{(3)} \end{bmatrix} + (u_{xx} + u_{yy}) \begin{bmatrix} 0 & 0 & \alpha_0^{(3)} & \alpha_1^{(3)} & \alpha_2^{(3)} \\ \alpha_3^{(3)} & \alpha_4^{(3)} & 0 & 0 & 0 \\ 0 & 0 & \alpha_5^{(3)} & \alpha_6^{(3)} & \alpha_7^{(3)} \end{bmatrix} \\
 & + (u_{xx} - u_{yy}) \begin{bmatrix} 0 & 0 & \beta_0^{(3)} & \beta_1^{(3)} & \beta_2^{(3)} \\ \beta_3^{(3)} & \beta_4^{(3)} & 0 & 0 & 0 \\ 0 & 0 & \beta_5^{(3)} & \beta_6^{(3)} & \beta_7^{(3)} \end{bmatrix} + (2u_{xy}) \begin{bmatrix} \beta_8^{(3)} & \beta_9^{(3)} & 0 & 0 & 0 \\ 0 & 0 & \beta_{10}^{(3)} & \beta_{11}^{(3)} & \beta_{12}^{(3)} \\ \beta_{13}^{(3)} & \beta_{14}^{(3)} & 0 & 0 & 0 \end{bmatrix}
 \end{aligned} \tag{12}$$

The (X₂-M) interaction, with reference bond from the origin to $2(\mathbf{a}_1 + \mathbf{a}_2)/3$, has the same form as the above with an overall (-1) factor. Finally, the (X₂-X₁) coupling has a reference vector $-2(\mathbf{a}_1 + \mathbf{a}_2)/3$, and the Hamiltonian takes the form:

$$H = \begin{bmatrix} t_8^{(3)} & 0 & t_{11}^{(3)} \\ 0 & t_9^{(3)} & 0 \\ t_{11}^{(3)} & 0 & t_{10}^{(3)} \end{bmatrix} + (u_{xx} + u_{yy}) \begin{bmatrix} \alpha_8^{(3)} & 0 & \alpha_{11}^{(3)} \\ 0 & \alpha_9^{(3)} & 0 \\ \alpha_{11}^{(3)} & 0 & \alpha_{10}^{(3)} \end{bmatrix} + (u_{xx} - u_{yy}) \begin{bmatrix} \beta_{15}^{(3)} & 0 & \beta_{18}^{(3)} \\ 0 & \beta_{16}^{(3)} & 0 \\ \beta_{18}^{(3)} & 0 & \beta_{17}^{(3)} \end{bmatrix} + (2u_{xy}) \begin{bmatrix} 0 & \beta_{19}^{(3)} & 0 \\ \beta_{19}^{(3)} & 0 & \beta_{20}^{(3)} \\ 0 & \beta_{20}^{(3)} & 0 \end{bmatrix} \tag{13}$$

For each of the above couplings in Eqs. (7)-(13) there are 2 additional symmetrically equivalent couplings related by $2\pi/3$ rotations (clockwise and counterclockwise). In order to implement these rotations on the tight-binding Hamiltonian, we use the following unitary transformations with $\phi = 2\pi/3$ to implement the counterclockwise rotation on p and d subspaces, respectively:

$$\mathcal{U}^X(\phi) = \begin{bmatrix} \cos \phi & \sin \phi & 0 \\ -\sin \phi & \cos \phi & 0 \\ 0 & 0 & 1 \end{bmatrix} \tag{14}$$

$$\mathcal{U}^M(\phi) = \begin{bmatrix} \cos 2\phi & 0 & -\sin 2\phi & 0 & 0 \\ 0 & \cos \phi & 0 & -\sin \phi & 0 \\ \sin 2\phi & 0 & \cos 2\phi & 0 & 0 \\ 0 & \sin \phi & 0 & \cos \phi & 0 \\ 0 & 0 & 0 & 0 & 1 \end{bmatrix} \tag{15}$$

Note that the orbital subspaces rotate in the opposite direction from the coordinate axes. The 2NN couplings

each have 3 additional symmetrically equivalent couplings related by a mirror symmetry in the xz -plane.

The strain-dependent tight-binding Hamiltonian for each material is specified by 163 parameters, which is significantly fewer than the 1056 parameters in a generic 11-dimensional Hamiltonian with isotropic and anisotropic strain dependence. Furthermore, these parameters are all extracted directly from the Wannier transformation of the DFT results (averaging over symmetrically equivalent terms) and are not the result of any fitting to the band structure. The parameters for each material are tabulated in the Appendix.

D. Work Function

The work function for each material is the difference in energy between the Fermi level of the TMDC and the vacuum (a location far from the TMDC layer): $\Delta\Phi = E_{\text{vac}} - E_F$. This can be easily extracted from the DFT to-

tal potential for each value of isotropic strain, and shows a mild (few percent) dependence on the strain, which can affect the diagonal ϵ values as well as the $\alpha^{(0)}$ couplings. The values reported in the tables in the Appendix have the strain dependent work function subtracted from the on-site couplings before fitting. The work function for the unstrained materials, which decreases with increasing atomic number of both the metal and the chalcogen atoms, was included in Table I.

E. Spin-Orbit Coupling

Atomic spin-orbit coupling (SOC) is described by the Hamiltonian $H_{\text{soc}} = \lambda_{\text{soc}} \mathbf{L} \cdot \mathbf{S}$. We can extract the value of λ_{soc} for each atomic species by considering the splitting between valence states in a single atom as calculated by DFT. Assuming the wavefunctions are eigenstates of \mathbf{J} , \mathbf{L} , and \mathbf{S} , the energy splitting is given by the difference between $j = \ell + 1/2$ and $j = \ell - 1/2$ states, namely $\Delta E_{\text{soc}} = \lambda_{\text{soc}}(\ell + 1/2)$. The value of λ_{soc} , in units of eV, is shown in Table III for the 6 species considered here.

TABLE III. The atomic spin-orbit coupling strength λ_{soc} , in units of eV.

	Ti	Nb	Ta	S	Se	Te
λ_{soc} (eV)	0.018	0.071	0.232	0.056	0.247	0.512

IV. MODEL VALIDATION

In this section we demonstrate the accuracy with which our strain-dependent TBH reproduces the DFT band structures. Fig. 3(a) shows that the band structure near the Fermi energy is captured by the 11-band Wannier transformation, because the bands calculated with DFT and those reconstructed from the full basis of Wannier functions show virtually no differences.

Our tight-binding model, however, ignores interactions beyond 3NN, and it is important to examine the extent to which neglecting those longer range couplings affects the band structure. Fig. 3(b) shows the 3NN TBH band structure along with the full Wannier reconstruction and a 5NN truncation. The qualitative band structures agree well, and the most significant quantitative differences appear in bands far from the Fermi level. These differences arise from the overlap with orbitals that are not included in our 11-band model. The Wannierization procedure used to calculate the MLWF includes the effects from these other states as longer range hopping terms, beyond even 5NN.

In Fig. 4, we show the effect of 2% isotropic compression and expansion on the band structure of TaSe₂. The black bands are the result of DFT calculations and the red bands are from our 3NN tight-binding model, demonstrating that our model tracks the decrease in

band dispersion as the crystal is expanded. From the tight-binding Hamiltonian it is easy to determine the irreducible representations of each band at the high symmetry points, Γ , M, K (see Fig. 4). Changing the lattice constant from 2% compression to 2% expansion results in the reordering of representations at the Γ -point near E_F , with the A_{1g} singlet rising up through first the E_u doublet (at the equilibrium lattice constant) and then the E_g doublet (at 2% expansion). This reordering is accurately captured by the tight-binding model. However, the band reordering at the K point caused by lattice expansion, with the singlet A_1 sinking below the E doublet, has already occurred in the DFT at the equilibrium lattice constant, whereas it requires a slight expansion in the lattice before it occurs in the tight-binding model.

We can also compare the TBH with the addition of atomic spin-orbit coupling to the DFT results. Specifically, we consider the three bands in TaSe₂ that lie just above E_F at Γ in the unstrained crystal. Figure 5 shows the change in energy as calculated within DFT (black) or using the tight-binding parametrization including atomic SOC: there is good quantitative agreement between the two approaches.

V. APPLICATIONS

There are many proposals for strain engineering of 2D materials. A 2D pattern of artificial atoms has been generated by draping a single layer of MoS₂ over a periodic array of nanocones in a substrate, creating regions of higher and lower biaxial strain [59]. More recently, draping a graphene sheet over a step edge in a copper substrate has been shown to produce 1D ripples along the direction of the step edge [60]. Lattice distortions also occur spontaneously in systems that undergo CDW reconstructions. Though these generally occur over much shorter length scales, for small distortions our strain model should be able to capture the most important effects. We demonstrate the usefulness and limitations of our strain-dependent tight-binding model for systems with non-uniform strain patterns by applying it to three example structures: a 1D sinusoidal ripple in TaS₂, the 2×2 CDW in TiSe₂, and the $\sqrt{13} \times \sqrt{13}$ CDW in TaS₂.

A. One-dimensional rippling

We have modeled the effects of long-wavelength lattice distortions on the electronic structure of TaS₂ subject to a sinusoidal strain of variable amplitude and wavelength in the x -direction. Our model accounts only for in-plane lattice distortions, which were shown to be important in reproducing the experimental data in Ref [60]. Our treatment here does not consider out of plane displacements.

To model a non-uniform strain pattern, we first create an atomic supercell that is large enough to include the

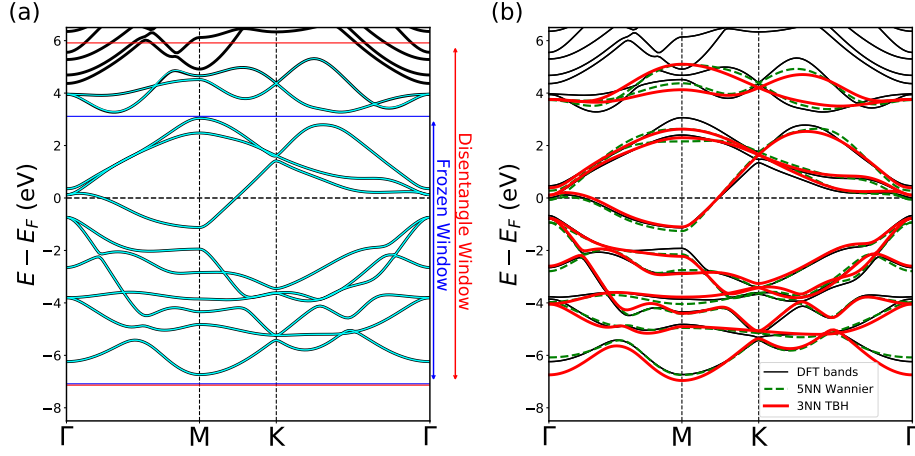


FIG. 3. (a) Comparison of the band structure calculated with DFT (black) and the full Wannier basis (cyan) for unstrained TaS₂. Also shown are the energy windows used to define the Wannier transformation and disentangle the bands arising from other orbitals [56, 58]. (b) Comparison of the band structure computed directly with DFT (thin black), 5NN Wannier basis (dashed green), and the 3NN TBH parametrization (thick red) for unstrained TaS₂.

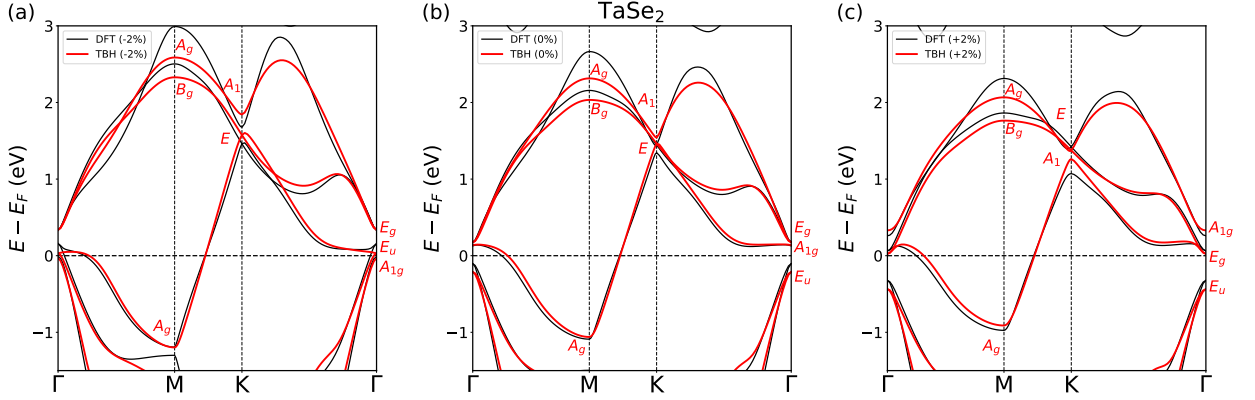


FIG. 4. Comparison of the band structure calculated using the 3NN TBH (red) and DFT (black) for a TaSe₂ crystal with three values of isotropic strain: (a) 2% compression, (b) unstrained, and (c) 2% expansion. The TBH bands are labeled by the irreducible representation of the symmetry group of the wave-vector at each high symmetry point. (Γ : D_{3d} , M: C_{2h} , K: D_3).

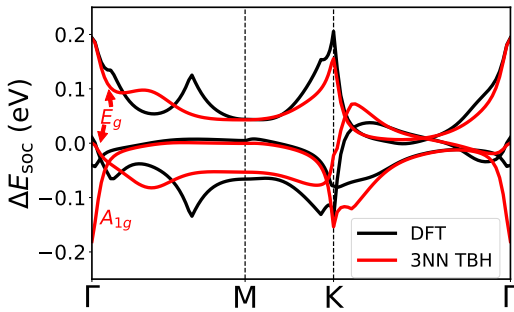


FIG. 5. Change in band energy due to spin-orbit coupling for three bands near the Fermi level in unstrained TaS₂. These bands can be identified as an A_{1g} singlet and E_g doublet at Γ . The difference in DFT calculated band energies with and without SOC, $\Delta E_{\text{SOC}} = E_{\text{with-soc}} - E_{\text{no-soc}}$, is shown in black, whereas the differences in tight-binding eigenvalues with and without SOC is shown in red.

entire periodic strain pattern. For the 1D ripple, we use a rectangular unit cell containing two formula units of TaS₂, and repeat it N times in the x -direction, as shown schematically in Fig. 6(a) for $N = 4$. Our model includes up to 3NN hopping, so each atom in the supercell interacts with 18 other atoms in addition to the on-site interaction. For each “bond” between interacting atoms we calculate the matrix elements in the Hamiltonian using our tight-binding parametrization with the components of the strain field evaluated at the center of the bond. This approximation ensures that the model Hamiltonian remains hermitian. For the 1D ripple the displacement field is $u(r) = A \sin(2\pi x/a\sqrt{3}N) \hat{x}$ and thus $u_{xx} = B \cos(2\pi x/a\sqrt{3}N)$ and $u_{yy} = u_{xy} = u_{yx} = 0$.

The supercell geometry and consequent folded band structure complicates the interpretation of the electronic structure. In this example our ripple has $2 \times 11 \times N$ bands. One way to make connections with the simpler

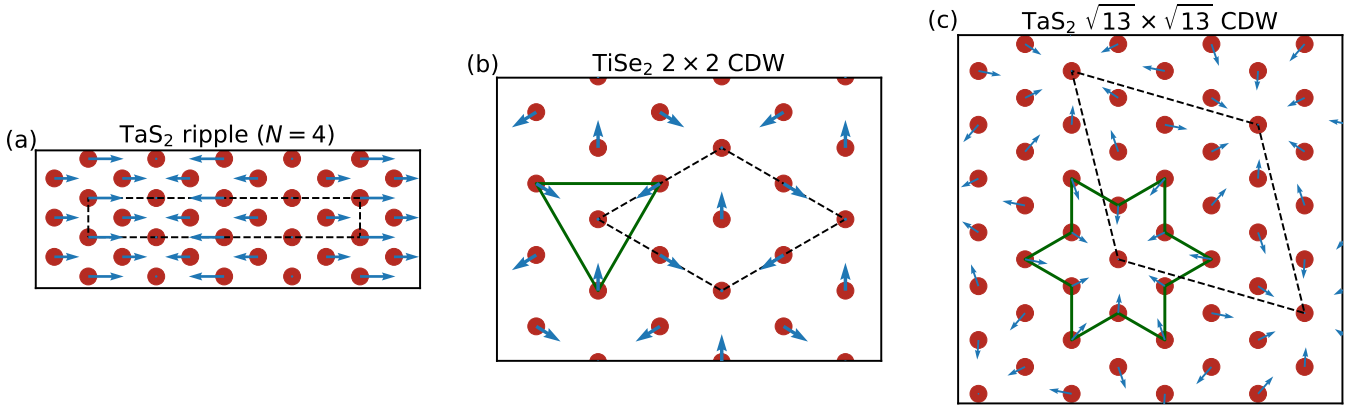


FIG. 6. The displacements of the metal atoms used in the applications of the strain-dependent TBH. (a) Sinusoidal strain in the x -direction with a period of $N = 4$ rectangular units. (b) 2×2 CDW pattern for TiSe_2 . (c) $\sqrt{13} \times \sqrt{13}$ CDW pattern for TaS_2 . The supercells are shown with dashed black lines, and the chalcogen atoms are omitted for clarity.

pristine crystal band structure is through an “unfolding procedure” to obtain the “effective band structure”. This method has been established to interpret the perturbations to the pristine band structure due to the presence of impurities, disordered alloys, and structural reconstructions in DFT calculations that use a supercell geometry [61–64]. The effective band structure can be further compared with the band structure derived from angle-resolved photoemission spectroscopy (ARPES).

In practice, the unfolding procedure is carried out with the proper crystal momentum projection based on the pristine unit cell, where the corresponding Fourier component determines the unfolding weight. Figure 7 shows the unfolded band structures for an $N = 4$ TaS_2 supercell both with and without the 1D sinusoidal strain. For comparison, we studied a supercell with displaced atoms directly using DFT, followed by the Wannier transformation and unfolding of the supercell band structure, and found only small differences. While in this case the DFT+Wannier calculation is not computationally prohibitive, it still takes several hours of CPU time for each configuration, and the resources required grow with the size of the supercell. By contrast, once the framework of the TBH supercell has been set up, the unfolded band structure can be produced much faster for any chosen amplitude or wavelength of the strain pattern, and for any of the 9 T-type TMDC materials we have modeled. Increasing the wavelength of the strain pattern to $\lambda = 93 \text{ \AA}$ ($N = 16$) results in a supercell with 96 atoms, which makes the DFT calculation very computationally demanding, while the TBH result, shown in Fig. 7(c), is obtained in under 1 minute using a laptop computer.

In T-TMDCs, CDW order is prevalent and affects the underlying electronic properties. Compared to the pristine crystal structure, the CDW order and electron-phonon couplings cause deformed and reconstructed atomic positions. For example, the T- TiSe_2 crystal exhibits a 2×2 reconstruction, while the T- TaS_2 crystal shows so-called Star-of-David deformations in the com-

mensurate CDW phase with a $\sqrt{13} \times \sqrt{13}$ supercell. We apply our TBH model to these situations next, and compare to DFT results when possible.

B. TiSe_2 CDW

For TiSe_2 we first build a 2×2 supercell, perturb the Ti atoms slightly, and use DFT to relax the positions of all atoms. The CDW indeed develops, with changes in the distances between the Ti atoms of $\pm 0.08 \text{ \AA}$, which is 2.3% of the optimized DFT lattice constant of 3.53 \AA . This amount of strain is at the upper limit of the uniform strain which we used to extract the parameters of the strain-dependent TBH and where the response in the TBH parameters was still quite linear. A schematic of the metal atom displacements is shown in Fig. 6(b). We match a continuous displacement field to the positions of the Ti atoms in the relaxed 2×2 supercell by fitting Fourier components of the first shell of reciprocal lattice vectors. The derivative of this displacement field is then used to determine the components of the strain field at the center of each bond between interacting atoms in the 2×2 supercell. Unlike the case of the 1D ripple, the TiSe_2 CDW strain pattern includes a non-zero antisymmetric scalar, ω_{xy} , which represents a local rotation. This is implemented in the TBH by rotating the strain-independent piece of the Hamiltonian for each bond by an angle $\phi = \omega_{xy}(x, y)$ evaluated at the center of each bond, using the matrices of Eqs. (14) and (15). Figure 8 shows the pristine and CDW-strained TiSe_2 bands unfolded to the primitive cell Brillouin zone. The opening of small gaps at the Fermi level is clearly captured, and the unfolded bands reproduce well those calculated directly with DFT+Wannier, shown in Fig 8(c).

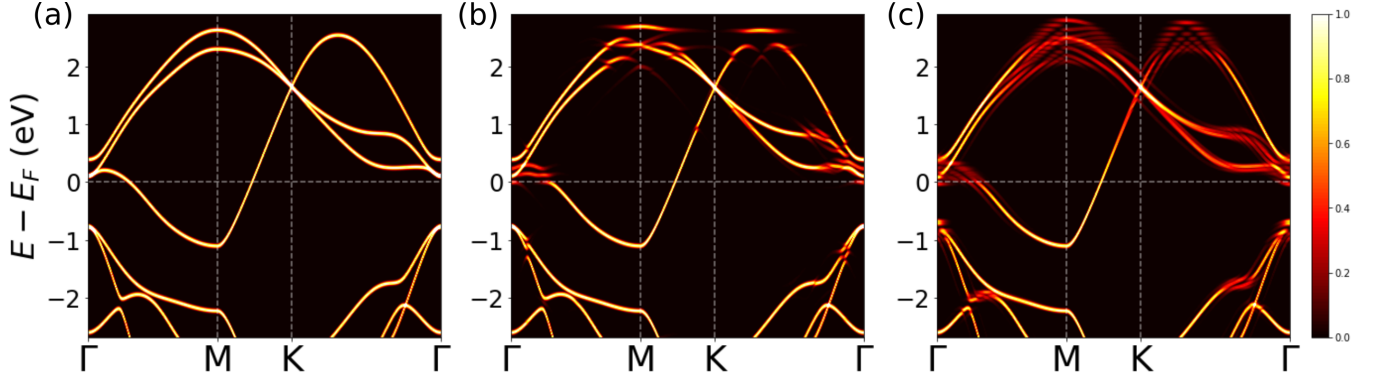


FIG. 7. Band structures for a $N \times 1$ rectangular supercell of TaS_2 , unfolded to a path in the Brillouin zone of the 3-atom primitive unit cell. (a) TBH bands for $N = 4$ without strain. (b) TBH bands for $N = 4$ subject to 1D sinusoidal strain with amplitude $B = 0.02$ and wavelength $\lambda = 23 \text{ \AA}$. (c) TBH bands for $N = 16$, subject to 1D sinusoidal strain with amplitude $B = 0.02$ and wavelength $\lambda = 93 \text{ \AA}$.

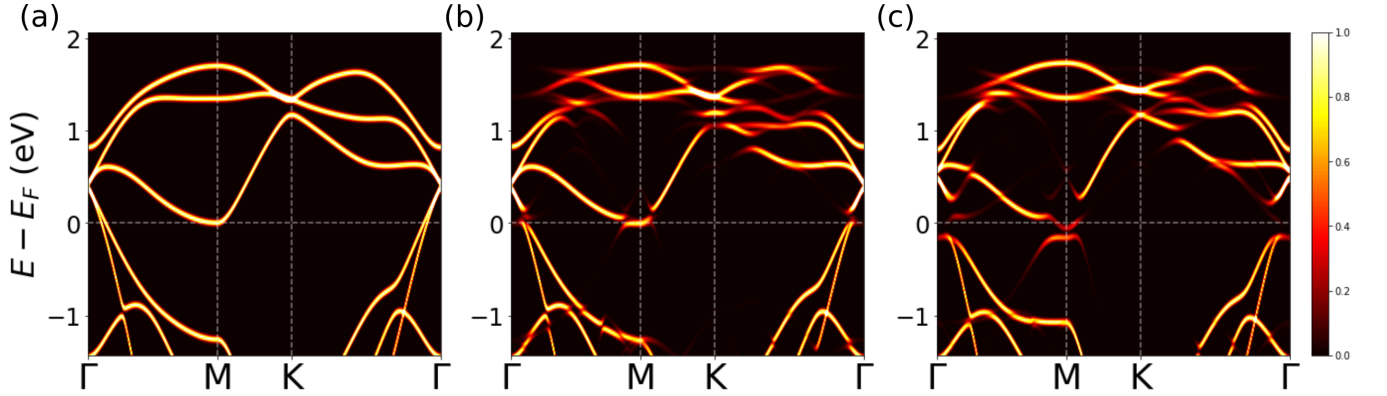


FIG. 8. Band structures for the 2×2 CDW supercell of TiSe_2 , unfolded to a path in the Brillouin zone of the 3-atom primitive unit cell. (a) TBH bands without the CDW distortion. (b) TBH bands for a strain pattern fit to the CDW displacements calculated with DFT. (c) DFT band structure for the relaxed CDW, for comparison.

C. TaS_2 CDW

The simple, symmetric model we have developed reveals its limitations when applied to the $\sqrt{13} \times \sqrt{13}$ CDW pattern that occurs in TaS_2 and TaSe_2 . For the former, relaxation of the supercell using DFT yields the experimentally observed CDW pattern, shown schematically in Fig. 6(c). The nearest Ta-Ta distances can increase by as much as 0.43 \AA while other distances decrease by up to 0.2 \AA , a range of -6% to $+13\%$ of the 3.36 \AA lattice constant. Displacements this large might be expected to exceed the linear strain regime parametrized in our model. Indeed, calculations using larger isotropic strains show that the response of one of the 1NN Ta-S couplings becomes very nonlinear, as shown in Fig. 9. Using the strain-dependent TBH to compute the electronic structure for the TaS_2 CDW in the same manner as for TiSe_2 , including local rotation ω and taking the strain field from a fit to the Ta positions in the relaxed DFT CDW structure, we see in Fig. 10 that many of the smaller features in the unfolded CDW band structure are well reproduced.

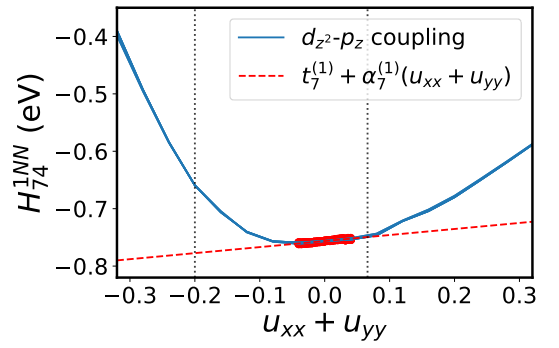


FIG. 9. Magnitude of the 1NN matrix element H_{74}^{1NN} , namely the $d_{z^2}-p_z$ coupling in TaS_2 , as a function of isotropic strain, $u_{xx} + u_{yy}$. The red points represent strain in the range $\pm 2\%$ used to produce the linear parametrization (red dashed line) for the strain-dependent TBH. The vertical dotted black lines indicate the range of isotropic strain occurring in the TaS_2 CDW pattern.

However, the TBH model fails to capture the significant flat band that emerges at Γ and is clearly visible in the DFT calculation, Fig. 10(c). In this case the perturbation from the pristine T-structure is so large that nonlinear effects in the strain response become important. The same is true for distorted phases such as the T'-structure (which has a dimerization of metal atoms in one direction). This is not a breakdown of the underlying procedure, for one can still use the Wannier transformation of the DFT results to construct accurate tight-binding models to study the coupling to acoustic phonons. However, the complexity increases significantly, preventing us from writing down simple, symmetric models.

VI. CONCLUSION

We have used the Wannier transformation of plane-wave DFT calculations to construct precise, strain-dependent tight-binding Hamiltonians for group-IV and group-V TMDCs that adopt the T-structure. We have further augmented the models with on-site spin orbit coupling terms and determined the work function for each material, providing a simple parametrization of the interaction of the electronic structure with long-wavelength acoustic phonons, which induce deformations of primitive vectors for the structural unit cell. Moreover, we have demonstrated how to model the short-wavelength CDW distortions with atomic displacements. The effects of such perturbations are visualized through the technique of band-structure unfolding. Similarly, the approach can be generalized to model crystals with internal atomic displacements due to optical phonons.

From a broader perspective, the strain response of single layers is a necessary ingredient for the construction of models of van der Waals heterostructures with multiple layers. These material systems have attracted attention recently since the discovery of unconventional correlated insulating and superconducting states in magic-angle twisted bilayer graphene [65–67]. In terms of its electronic structure modeling, the layer deformation and strain from the mechanical relaxations in a twisted bilayer are shown to be relevant in modifying the electronic structure when compared with experimental observations [68]. Our modeling of single layers with strain paves the way for investigating heterostructures involving diverse types of T-TMDCs and the interplay between different order parameters. The other crucial ingredient necessary for a comprehensive, single-particle model of the electronic structure, is the proper interlayer couplings between orbitals in adjacent layers [69, 70]. This will be explored in future work.

ACKNOWLEDGMENTS

We thank Stephen Carr, Jhih-Shih You, Dennis Huang, and Philip Kim for useful discussions. This work

was supported by the STC Center for Integrated Quantum Materials, NSF Grant No. DMR-1231319 and by ARO MURI Award W911NF-14-0247. S.F. is supported by a Rutgers Center for Material Theory Distinguished Postdoctoral Fellowship. S.B.T. and J.C. recognize the support of the DOE Computational Science Graduate Fellowship (CSGF) under grant DE-FG02-97ER25308. This work used the Stampede2 supercomputer at the Texas Advanced Computing Center through allocation TG-DMR120073, which is part of the Extreme Science and Engineering Discovery Environment (XSEDE), supported by NSF Grant No. ACI-1548562. We also used the Odyssey cluster supported by the FAS Division of Science, Research Computing Group at Harvard University.

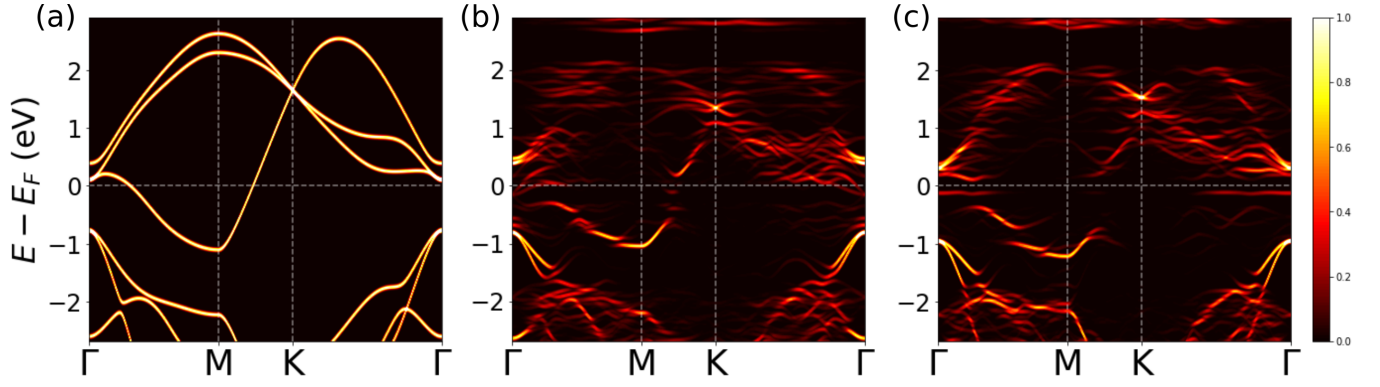


FIG. 10. Band structures for the $\sqrt{13} \times \sqrt{13}$ CDW supercell of TaS₂, unfolded to a path in the Brillouin zone of the 3-atom primitive unit cell. (a) TBH bands without the CDW distortion, (b) TBH bands for a strain pattern fit to the CDW displacements calculated with DFT, and (c) DFT band structure for the relaxed CDW.

Appendix A T-TMDC STRAIN-DEPENDENT TIGHT-BINDING PARAMETERS

TABLE IV. T-type TMDC onsite strain terms in units of eV.

	TiS ₂	TiSe ₂	TiTe ₂	NbS ₂	NbSe ₂	NbTe ₂	TaS ₂	TaSe ₂	TaTe ₂
ϵ_0	-10.093	-9.195	-7.117	-9.023	-8.126	-6.178	-9.444	-8.582	-6.595
ϵ_1	-10.030	-9.238	-7.324	-9.120	-8.322	-6.582	-9.532	-8.767	-7.041
ϵ_2	-7.441	-6.809	-5.080	-6.523	-5.950	-4.413	-6.374	-5.906	-4.443
ϵ_3	-7.072	-6.468	-4.776	-5.725	-5.256	-3.855	-5.375	-5.034	-3.706
ϵ_4	-7.676	-6.998	-5.269	-6.803	-6.192	-4.694	-6.700	-6.197	-4.753
ϵ_5	-0.442	-0.359	-0.304	-0.680	-0.548	-0.459	-0.779	-0.636	-0.511
$\alpha_0^{(0)}$	-5.791	-5.989	-7.350	-5.618	-4.835	-6.604	-5.162	-5.132	-4.924
$\alpha_1^{(0)}$	-3.771	-3.816	-4.825	-4.046	-3.126	-4.564	-3.080	-2.837	-2.251
$\alpha_2^{(0)}$	-6.723	-6.992	-8.206	-5.086	-4.600	-6.592	-4.074	-4.568	-4.210
$\alpha_3^{(0)}$	-8.008	-8.008	-8.649	-6.718	-5.818	-6.767	-6.918	-6.695	-5.945
$\alpha_4^{(0)}$	-6.659	-6.855	-7.738	-4.898	-4.406	-5.744	-4.175	-4.368	-4.199
$\alpha_5^{(0)}$	0.408	0.301	0.196	0.245	0.137	0.130	-0.052	-0.052	-0.275
$\beta_0^{(0)}$	-0.642	-0.604	-0.692	-0.477	-0.423	-0.589	-0.045	-0.033	-0.349
$\beta_1^{(0)}$	0.410	0.505	0.594	0.355	0.553	0.715	1.164	1.360	1.262
$\beta_2^{(0)}$	0.476	0.367	0.251	0.576	0.445	0.342	0.403	0.255	0.096
$\beta_3^{(0)}$	0.322	0.334	0.338	0.472	0.526	0.556	1.033	1.138	0.979
$\beta_4^{(0)}$	-0.554	-0.497	-0.334	-0.623	-0.450	-0.071	-0.609	-0.463	-0.032
$\beta_5^{(0)}$	-0.195	-0.167	-0.128	-0.227	-0.173	-0.202	-0.112	-0.036	0.009
$\beta_6^{(0)}$	-0.101	-0.131	-0.114	-0.041	-0.049	0.037	0.183	0.198	0.205

TABLE V. T-type TMDC 1NN isotropic strain terms in units of eV.

	TiS ₂	TiSe ₂	TiTe ₂	NbS ₂	NbSe ₂	NbTe ₂	TaS ₂	TaSe ₂	TaTe ₂
$t_0^{(1)}$	0.530	0.433	0.322	0.548	0.448	0.326	0.534	0.447	0.293
$t_1^{(1)}$	1.252	1.122	0.962	1.537	1.378	1.182	1.626	1.463	1.252
$t_2^{(1)}$	0.386	0.386	0.391	0.555	0.543	0.547	0.549	0.511	0.508
$t_3^{(1)}$	-0.698	-0.635	-0.565	-0.847	-0.772	-0.694	-0.925	-0.842	-0.766
$t_4^{(1)}$	-0.493	-0.441	-0.376	-0.597	-0.532	-0.437	-0.631	-0.559	-0.450
$t_5^{(1)}$	0.811	0.729	0.601	0.978	0.885	0.724	0.985	0.892	0.699
$t_6^{(1)}$	0.479	0.500	0.465	0.778	0.788	0.709	0.773	0.772	0.677
$t_7^{(1)}$	-0.574	-0.507	-0.423	-0.667	-0.586	-0.470	-0.756	-0.684	-0.575
$t_8^{(1)}$	0.220	0.201	0.194	0.145	0.135	0.128	0.190	0.186	0.179
$t_9^{(1)}$	-0.112	-0.102	-0.065	-0.127	-0.110	-0.052	-0.175	-0.169	-0.100
$t_{10}^{(1)}$	0.430	0.454	0.455	0.356	0.395	0.409	0.390	0.432	0.428
$t_{11}^{(1)}$	-0.363	-0.349	-0.292	-0.262	-0.262	-0.208	-0.285	-0.295	-0.228
$\alpha_0^{(1)}$	0.667	0.634	0.568	0.914	0.850	0.669	1.520	1.341	1.695
$\alpha_1^{(1)}$	-0.659	-0.454	-0.257	-0.380	-0.153	-0.032	-0.362	-0.221	-0.049
$\alpha_2^{(1)}$	-1.169	-1.002	-0.888	-1.274	-1.085	-0.945	-1.187	-1.033	-0.779
$\alpha_3^{(1)}$	0.750	0.624	0.516	0.538	0.396	0.302	0.927	0.785	0.709
$\alpha_4^{(1)}$	0.363	0.271	0.095	0.203	0.097	-0.121	-0.168	-0.189	-0.744
$\alpha_5^{(1)}$	-0.407	-0.289	-0.124	-0.175	-0.065	0.015	0.183	0.220	0.621
$\alpha_6^{(1)}$	-1.381	-1.214	-0.864	-1.750	-1.506	-1.052	-1.791	-1.513	-1.274
$\alpha_7^{(1)}$	0.281	0.187	0.025	-0.116	-0.210	-0.363	0.105	0.056	-0.076
$\alpha_8^{(1)}$	0.550	0.526	0.523	0.395	0.418	0.438	0.511	0.526	0.551
$\alpha_9^{(1)}$	-0.435	-0.420	-0.425	-0.413	-0.403	-0.388	-0.533	-0.515	-0.462
$\alpha_{10}^{(1)}$	-0.001	0.040	0.083	0.037	0.047	0.074	0.134	0.141	0.232
$\alpha_{11}^{(1)}$	-0.625	-0.617	-0.639	-0.539	-0.538	-0.551	-0.747	-0.746	-0.742

TABLE VI. T-type TMDC 1NN anisotropic strain terms in units of eV.

	TiS ₂	TiSe ₂	TiTe ₂	NbS ₂	NbSe ₂	NbTe ₂	TaS ₂	TaSe ₂	TaTe ₂
$\beta_0^{(1)}$	0.129	0.193	0.208	0.423	0.482	0.445	1.069	1.102	0.805
$\beta_1^{(1)}$	-0.320	-0.115	0.019	0.071	0.282	0.294	1.094	1.197	0.952
$\beta_2^{(1)}$	-1.185	-1.115	-0.994	-1.398	-1.283	-1.125	-1.340	-1.191	-1.119
$\beta_3^{(1)}$	1.026	0.883	0.751	1.056	0.925	0.818	1.150	1.002	0.889
$\beta_4^{(1)}$	0.670	0.594	0.467	0.849	0.724	0.532	1.034	0.923	0.665
$\beta_5^{(1)}$	-0.736	-0.573	-0.326	-0.673	-0.441	-0.140	-0.336	-0.116	0.091
$\beta_6^{(1)}$	-0.400	-0.327	-0.242	-0.505	-0.335	-0.234	0.125	0.287	0.278
$\beta_7^{(1)}$	0.530	0.409	0.309	0.470	0.350	0.264	0.722	0.662	0.552
$\beta_8^{(1)}$	1.283	1.139	0.986	1.538	1.413	1.168	1.674	1.460	1.094
$\beta_9^{(1)}$	-0.263	-0.376	-0.430	-0.605	-0.762	-0.769	-1.513	-1.632	-1.380
$\beta_{10}^{(1)}$	0.792	0.672	0.515	0.867	0.742	0.551	0.807	0.670	0.492
$\beta_{11}^{(1)}$	0.530	0.444	0.272	0.626	0.512	0.275	0.424	0.283	0.083
$\beta_{12}^{(1)}$	0.119	0.125	0.132	0.270	0.237	0.256	0.219	0.180	0.143
$\beta_{13}^{(1)}$	0.752	0.707	0.591	1.079	1.035	0.809	1.028	0.926	0.648
$\beta_{14}^{(1)}$	-0.138	-0.209	-0.172	-0.349	-0.449	-0.296	-0.965	-1.137	-0.733
$\beta_{15}^{(1)}$	0.189	0.221	0.196	0.289	0.327	0.223	0.304	0.336	0.238
$\beta_{16}^{(1)}$	0.086	0.032	0.011	-0.105	-0.175	-0.112	-0.360	-0.430	-0.300
$\beta_{17}^{(1)}$	-0.371	-0.279	-0.221	-0.141	-0.028	-0.079	-0.236	-0.141	-0.212
$\beta_{18}^{(1)}$	0.028	-0.064	-0.161	-0.230	-0.327	-0.375	-0.336	-0.398	-0.407
$\beta_{19}^{(1)}$	0.080	0.074	0.033	0.107	0.081	0.031	0.192	0.169	0.076
$\beta_{20}^{(1)}$	-0.313	-0.287	-0.264	-0.155	-0.133	-0.108	-0.107	-0.092	-0.028

TABLE VII. T-type TMDC 2NN isotropic strain terms in units of eV.

	TiS ₂	TiSe ₂	TiTe ₂	NbS ₂	NbSe ₂	NbTe ₂	TaS ₂	TaSe ₂	TaTe ₂
$t_0^{(2)}$	-0.067	-0.072	-0.040	-0.087	-0.089	-0.039	-0.077	-0.081	-0.026
$t_1^{(2)}$	0.701	0.782	0.883	0.732	0.831	0.982	0.762	0.842	0.989
$t_2^{(2)}$	-0.113	-0.137	-0.162	-0.159	-0.187	-0.219	-0.153	-0.176	-0.200
$t_3^{(2)}$	-0.050	-0.051	-0.051	-0.047	-0.048	-0.040	-0.076	-0.080	-0.071
$t_4^{(2)}$	0.015	0.019	0.030	0.039	0.040	0.046	0.062	0.065	0.072
$t_5^{(2)}$	-0.018	-0.034	-0.034	-0.036	-0.049	-0.037	-0.067	-0.085	-0.066
$t_6^{(2)}$	0.032	0.056	0.072	0.140	0.169	0.182	0.188	0.199	0.229
$t_7^{(2)}$	-0.125	-0.091	-0.074	-0.188	-0.121	-0.085	-0.205	-0.140	-0.079
$t_8^{(2)}$	-0.214	-0.201	-0.188	-0.467	-0.432	-0.398	-0.547	-0.486	-0.453
$t_9^{(2)}$	-0.021	-0.016	-0.004	-0.006	-0.005	0.011	-0.028	-0.028	-0.007
$t_{10}^{(2)}$	-0.103	-0.108	-0.113	-0.267	-0.263	-0.254	-0.313	-0.297	-0.304
$t_{11}^{(2)}$	0.210	0.166	0.141	0.339	0.265	0.225	0.365	0.282	0.222
$t_{12}^{(2)}$	0.114	0.088	0.070	0.158	0.117	0.082	0.162	0.121	0.074
$t_{13}^{(2)}$	-0.196	-0.182	-0.170	-0.387	-0.351	-0.316	-0.445	-0.395	-0.368
$t_{14}^{(2)}$	0.094	0.077	0.058	0.126	0.096	0.053	0.147	0.116	0.063
$\alpha_0^{(2)}$	0.059	0.036	-0.115	0.039	0.012	-0.168	-0.046	-0.076	-0.197
$\alpha_1^{(2)}$	-1.344	-1.493	-1.681	-1.329	-1.523	-1.822	-1.256	-1.403	-1.744
$\alpha_2^{(2)}$	0.408	0.464	0.548	0.493	0.557	0.672	0.396	0.438	0.534
$\alpha_3^{(2)}$	-0.104	-0.102	-0.118	-0.132	-0.130	-0.135	-0.191	-0.192	-0.138
$\alpha_4^{(2)}$	-0.030	-0.023	-0.014	-0.077	-0.053	-0.005	-0.039	-0.030	0.028
$\alpha_5^{(2)}$	0.020	0.018	-0.031	-0.104	-0.088	-0.129	-0.114	-0.103	-0.176
$\alpha_6^{(2)}$	-0.581	-0.576	-0.536	-1.242	-1.177	-1.038	-1.608	-1.394	-1.389
$\alpha_7^{(2)}$	0.128	-0.006	-0.135	-0.258	-0.452	-0.529	-0.146	-0.296	-0.264
$\alpha_8^{(2)}$	0.944	0.835	0.722	1.608	1.418	1.188	1.885	1.613	1.387
$\alpha_9^{(2)}$	-0.202	-0.154	-0.119	-0.357	-0.248	-0.187	-0.422	-0.276	-0.291
$\alpha_{10}^{(2)}$	0.677	0.638	0.568	1.200	1.099	0.863	1.480	1.335	1.255
$\alpha_{11}^{(2)}$	-0.383	-0.284	-0.223	-0.292	-0.205	-0.192	-0.140	-0.125	-0.061
$\alpha_{12}^{(2)}$	-0.069	-0.024	0.031	0.127	0.163	0.202	0.377	0.341	0.604
$\alpha_{13}^{(2)}$	0.727	0.622	0.503	1.028	0.851	0.599	1.260	1.074	0.882
$\alpha_{14}^{(2)}$	-0.047	-0.000	0.089	0.227	0.253	0.351	0.389	0.372	0.649

TABLE VIII. T-type TMDC 2NN anisotropic strain terms in units of eV.

	TiS ₂	TiSe ₂	TiTe ₂	NbS ₂	NbSe ₂	NbTe ₂	TaS ₂	TaSe ₂	TaTe ₂
$\beta_0^{(2)}$	-0.516	-0.570	-0.718	-0.544	-0.616	-0.839	-0.541	-0.595	-0.798
$\beta_1^{(2)}$	1.656	1.835	2.106	1.734	1.965	2.356	1.854	2.025	2.371
$\beta_2^{(2)}$	-0.439	-0.502	-0.573	-0.574	-0.655	-0.721	-0.526	-0.584	-0.592
$\beta_3^{(2)}$	-0.100	-0.121	-0.121	-0.152	-0.191	-0.151	-0.286	-0.320	-0.246
$\beta_4^{(2)}$	0.085	0.088	0.081	0.170	0.172	0.113	0.149	0.133	0.101
$\beta_5^{(2)}$	-0.024	-0.063	-0.035	-0.057	-0.119	-0.052	-0.175	-0.243	-0.150
$\beta_6^{(2)}$	0.475	0.524	0.610	0.489	0.561	0.705	0.521	0.577	0.731
$\beta_7^{(2)}$	0.034	0.023	0.027	0.036	0.020	0.027	0.137	0.130	0.129
$\beta_8^{(2)}$	-0.010	-0.021	-0.039	-0.008	-0.038	-0.074	-0.054	-0.088	-0.140
$\beta_9^{(2)}$	0.315	0.332	0.341	0.820	0.780	0.727	1.128	1.031	1.000
$\beta_{10}^{(2)}$	0.160	0.175	0.158	0.601	0.566	0.482	0.546	0.441	0.472
$\beta_{11}^{(2)}$	-0.922	-0.758	-0.622	-1.406	-1.140	-0.947	-1.544	-1.260	-1.187
$\beta_{12}^{(2)}$	0.019	0.002	-0.005	-0.066	-0.101	-0.120	-0.382	-0.410	-0.413
$\beta_{13}^{(2)}$	-0.233	-0.205	-0.152	-0.376	-0.340	-0.224	-0.446	-0.431	-0.381
$\beta_{14}^{(2)}$	0.464	0.357	0.269	0.516	0.389	0.272	0.474	0.363	0.182
$\beta_{15}^{(2)}$	0.127	0.100	0.037	0.121	0.103	-0.020	0.203	0.218	-0.028
$\beta_{16}^{(2)}$	-0.552	-0.470	-0.378	-0.868	-0.716	-0.540	-0.958	-0.812	-0.684
$\beta_{17}^{(2)}$	0.067	0.068	0.049	0.152	0.154	0.075	0.350	0.372	0.262
$\beta_{18}^{(2)}$	0.216	0.221	0.198	0.545	0.544	0.478	0.641	0.612	0.516
$\beta_{19}^{(2)}$	-0.130	-0.120	-0.145	-0.235	-0.220	-0.276	-0.312	-0.272	-0.339
$\beta_{20}^{(2)}$	0.167	0.149	0.117	0.392	0.365	0.281	0.394	0.339	0.248
$\beta_{21}^{(2)}$	-0.006	-0.013	-0.016	-0.061	-0.088	-0.086	-0.141	-0.144	-0.137
$\beta_{22}^{(2)}$	-0.076	-0.048	-0.030	-0.027	0.008	0.030	0.153	0.199	0.182
$\beta_{23}^{(2)}$	-0.161	-0.151	-0.111	-0.390	-0.368	-0.255	-0.451	-0.399	-0.220

TABLE IX. T-type TMDC 3NN isotropic strain terms in units of eV.

	TiS ₂	TiSe ₂	TiTe ₂	NbS ₂	NbSe ₂	NbTe ₂	TaS ₂	TaSe ₂	TaTe ₂
$t_0^{(3)}$	-0.055	-0.054	-0.058	-0.077	-0.071	-0.075	-0.087	-0.078	-0.082
$t_1^{(3)}$	0.018	0.008	-0.014	-0.005	-0.015	-0.052	-0.016	-0.024	-0.067
$t_2^{(3)}$	0.037	0.051	0.063	0.093	0.107	0.120	0.095	0.102	0.109
$t_3^{(3)}$	-0.057	-0.052	-0.064	-0.048	-0.042	-0.061	-0.086	-0.079	-0.098
$t_4^{(3)}$	0.022	0.020	0.048	0.046	0.041	0.083	0.088	0.076	0.131
$t_5^{(3)}$	0.011	0.027	0.034	0.049	0.070	0.085	0.037	0.054	0.073
$t_6^{(3)}$	-0.060	-0.057	-0.083	-0.091	-0.089	-0.130	-0.125	-0.115	-0.163
$t_7^{(3)}$	0.014	0.008	0.000	-0.016	-0.023	-0.037	-0.013	-0.014	-0.025
$t_8^{(3)}$	-0.040	-0.041	-0.051	-0.044	-0.046	-0.055	-0.009	-0.011	-0.020
$t_9^{(3)}$	-0.086	-0.080	-0.068	-0.131	-0.119	-0.098	-0.153	-0.144	-0.123
$t_{10}^{(3)}$	-0.072	-0.073	-0.065	-0.089	-0.089	-0.061	-0.054	-0.050	-0.005
$t_{11}^{(3)}$	0.028	0.024	0.015	0.065	0.057	0.054	0.119	0.112	0.116
$\alpha_0^{(3)}$	0.314	0.266	0.233	0.242	0.194	0.169	0.334	0.276	0.119
$\alpha_1^{(3)}$	0.122	0.118	0.172	0.259	0.227	0.290	0.413	0.362	0.373
$\alpha_2^{(3)}$	-0.411	-0.429	-0.426	-0.520	-0.528	-0.492	-0.607	-0.614	-0.491
$\alpha_3^{(3)}$	0.024	0.009	-0.006	-0.097	-0.101	-0.117	-0.171	-0.139	-0.257
$\alpha_4^{(3)}$	-0.220	-0.201	-0.234	-0.301	-0.245	-0.216	-0.477	-0.447	-0.321
$\alpha_5^{(3)}$	-0.273	-0.317	-0.366	-0.423	-0.484	-0.571	-0.494	-0.525	-0.681
$\alpha_6^{(3)}$	0.323	0.306	0.345	0.377	0.352	0.313	0.528	0.511	0.414
$\alpha_7^{(3)}$	0.184	0.211	0.246	0.293	0.330	0.363	0.368	0.400	0.389
$\alpha_8^{(3)}$	0.054	0.051	0.068	0.088	0.094	0.112	0.073	0.115	0.086
$\alpha_9^{(3)}$	0.085	0.052	0.012	0.014	-0.034	-0.082	-0.006	-0.037	-0.095
$\alpha_{10}^{(3)}$	0.088	0.097	0.053	0.005	0.023	-0.018	-0.228	-0.232	-0.233
$\alpha_{11}^{(3)}$	-0.044	-0.022	-0.009	-0.065	-0.014	0.033	-0.220	-0.184	-0.118

TABLE X. T-type TMDC 3NN anisotropic strain terms in units of eV.

	TiS ₂	TiSe ₂	TiTe ₂	NbS ₂	NbSe ₂	NbTe ₂	TaS ₂	TaSe ₂	TaTe ₂
$\beta_0^{(3)}$	0.524	0.515	0.559	0.625	0.593	0.674	0.709	0.668	0.708
$\beta_1^{(3)}$	-0.461	-0.424	-0.318	-0.565	-0.518	-0.333	-0.473	-0.427	-0.236
$\beta_2^{(3)}$	-0.096	-0.105	-0.095	-0.098	-0.102	-0.067	-0.111	-0.117	-0.074
$\beta_3^{(3)}$	-0.012	-0.015	-0.010	-0.085	-0.079	-0.061	-0.193	-0.184	-0.121
$\beta_4^{(3)}$	-0.135	-0.125	-0.136	-0.191	-0.175	-0.186	-0.092	-0.049	-0.096
$\beta_5^{(3)}$	-0.004	-0.054	-0.079	-0.051	-0.113	-0.159	0.006	-0.063	-0.138
$\beta_6^{(3)}$	0.240	0.231	0.238	0.327	0.314	0.333	0.489	0.438	0.457
$\beta_7^{(3)}$	0.110	0.133	0.178	0.234	0.256	0.305	0.306	0.318	0.376
$\beta_8^{(3)}$	0.158	0.138	0.160	0.223	0.209	0.284	0.249	0.228	0.271
$\beta_9^{(3)}$	0.073	0.076	0.005	0.178	0.144	-0.035	0.210	0.174	-0.053
$\beta_{10}^{(3)}$	-0.227	-0.226	-0.258	-0.330	-0.311	-0.339	-0.452	-0.426	-0.423
$\beta_{11}^{(3)}$	0.115	0.108	0.093	0.118	0.118	0.096	0.024	0.010	0.004
$\beta_{12}^{(3)}$	0.148	0.159	0.204	0.189	0.202	0.270	0.227	0.232	0.293
$\beta_{13}^{(3)}$	-0.120	-0.106	-0.131	-0.150	-0.132	-0.190	-0.290	-0.270	-0.261
$\beta_{14}^{(3)}$	-0.015	-0.018	0.010	0.003	0.004	0.078	0.138	0.159	0.174
$\beta_{15}^{(3)}$	-0.351	-0.350	-0.288	-0.560	-0.574	-0.419	-1.296	-1.281	-0.934
$\beta_{16}^{(3)}$	0.177	0.155	0.131	0.242	0.211	0.174	0.305	0.278	0.250
$\beta_{17}^{(3)}$	-0.036	-0.075	-0.105	-0.116	-0.189	-0.235	-0.336	-0.401	-0.365
$\beta_{18}^{(3)}$	-0.306	-0.308	-0.266	-0.508	-0.538	-0.461	-0.956	-0.979	-0.791
$\beta_{19}^{(3)}$	0.041	0.042	0.042	0.095	0.110	0.104	0.162	0.179	0.185
$\beta_{20}^{(3)}$	-0.030	-0.044	-0.026	-0.034	-0.042	0.011	-0.003	-0.013	0.066

-
- [1] S. Fang, S. Carr, M. A. Cazalilla, and E. Kaxiras, Electronic structure theory of strained two-dimensional materials with hexagonal symmetry, *Phys. Rev. B* **98**, 075106 (2018).
- [2] A. K. Geim and I. V. Grigorieva, Van der Waals heterostructures, *Nature* **499**, 419 (2013).
- [3] Q. H. Wang, K. Kalantar-Zadeh, A. Kis, J. N. Coleman, and M. S. Strano, Electronics and optoelectronics of two-dimensional transition metal dichalcogenides, *Nat Nano* **7**, 699 (2012).
- [4] N. Zibouche, A. Kuc, J. Musfeldt, and T. Heine, Transition-metal dichalcogenides for spintronic applications, *Annalen der Physik* **526**, 395 (2014).
- [5] X. Xu, W. Yao, D. Xiao, and T. F. Heinz, Spin and pseudospins in layered transition metal dichalcogenides, *Nat Phys* **10**, 343 (2014).
- [6] M. T. Ong and E. J. Reed, Engineered piezoelectricity in graphene, *ACS Nano* **6**, 1387 (2012).
- [7] A. A. Bukharaev, A. K. Zvezdin, A. P. Pyatakov, and Y. K. Fetisov, Straintronics: a new trend in micro- and nanoelectronics and materials science, *Physics-Uspekhi* **61**, 1175 (2018).
- [8] S. Carr, D. Massatt, S. Fang, P. Cazeaux, M. Luskin, and E. Kaxiras, Twistronics: Manipulating the electronic properties of two-dimensional layered structures through their twist angle, *Phys. Rev. B* **95**, 075420 (2017).
- [9] J. Lee, Z. Wang, K. He, J. Shan, and P. X.-L. Feng, High frequency MoS₂ nanomechanical resonators, *ACS Nano* **7**, 6086 (2013).
- [10] R. E. Groenewald, M. Rösner, G. Schönhoff, S. Haas, and T. O. Wehling, Valley plasmonics in transition metal dichalcogenides, *Phys. Rev. B* **93**, 205145 (2016).
- [11] T. Ritschel, J. Trinckauf, K. Koepf, B. Büchner, M. v. Zimmermann, H. Berger, Y. Joe, P. Abbamonte, and J. Geck, Orbital textures and charge density waves in transition metal dichalcogenides, *Nat. Phys.* **11**, 328 (2015).
- [12] J. T. Ye, Y. J. Zhang, R. Akashi, M. S. Bahramy, R. Arita, and Y. Iwasa, Superconducting dome in a gate-tuned band insulator, *Science* **338**, 1193 (2012).
- [13] J. Zhang, J. M. Soon, K. P. Loh, J. Yin, J. Ding, M. B. Sullivan, and P. Wu, Magnetic molybdenum disulfide nanosheet films, *Nano Letters* **7**, 2370 (2007).
- [14] C. Gong, L. Li, Z. Li, H. Ji, A. Stern, Y. Xia, T. Cao, W. Bao, C. Wang, Y. Wang, Z. Q. Qiu, R. J. Cava, S. G. Louie, J. Xia, and X. Zhang, Discovery of intrinsic ferromagnetism in two-dimensional van der Waals crystals, *Nature* **546**, 265 EP (2017).
- [15] B. Huang, G. Clark, E. Navarro-Moratalla, D. R. Klein, R. Cheng, K. L. Seyler, D. Zhong, E. Schmidgall, M. A. McGuire, D. H. Cobden, W. Yao, D. Xiao, P. Jarillo-Herrero, and X. Xu, Layer-dependent ferromagnetism in a van der Waals crystal down to the monolayer limit, *Nature* **546**, 270 EP (2017).
- [16] X. Qian, J. Liu, L. Fu, and J. Li, Quantum spin hall effect in two-dimensional transition metal dichalcogenides, *Science* **346**, 1344 (2014).
- [17] S. Wu, V. Fatemi, Q. D. Gibson, K. Watanabe, T. Taniguchi, R. J. Cava, and P. Jarillo-Herrero, Observation of the quantum spin hall effect up to 100 Kelvin in a monolayer crystal, *Science* **359**, 76 (2018).
- [18] Y. Nakata, K. Sugawara, R. Shimizu, Y. Okada, P. Han, T. Hitosugi, K. Ueno, T. Sato, and T. Takahashi, Monolayer 1T-NbSe₂ as a Mott insulator, *NPG Asia Mater.* **8**, e321 (2016).
- [19] L. Ma, C. Ye, Y. Yu, X. F. Lu, X. Niu, S. Kim, D. Feng, D. Tománek, Y.-W. Son, X. H. Chen, and Y. Zhang, A metallic mosaic phase and the origin of Mott-insulating state in 1T-TaS₂, *Nature Communications* **7**, 10956 EP (2016).
- [20] K. T. Law and P. A. Lee, 1T-TaS₂ as a quantum spin liquid, *Proceedings of the National Academy of Sciences* **114**, 6996 (2017).
- [21] H.-S. Kim, K. Haule, and D. Vanderbilt, Mott metal-insulator transitions in pressurized layered trichalcogenides, *Phys. Rev. Lett.* **123**, 236401 (2019).
- [22] A. W. Tsen, R. Hovden, D. Wang, Y. D. Kim, J. Okamoto, K. A. Spoth, Y. Liu, W. Lu, Y. Sun, J. C. Hone, L. K. Kourkoutis, P. Kim, and A. N. Pasupathy, Structure and control of charge density waves in two-dimensional 1T-TaS₂, *Proc. Natl. Acad. Sci.* **112**, 15054 (2015).
- [23] B. Sipoš, A. F. Kusmartseva, A. Akrap, H. Berger, L. Forró, and E. Tutiš, From Mott state to superconductivity in 1T-TaS₂, *Nat. Mater.* **7**, 960 (2008).
- [24] R. Murray and A. Yoffe, The band structures of some transition metal dichalcogenides: band structures of the titanium dichalcogenides, *Journal of Physics C: Solid State Physics* **5**, 3038 (1972).
- [25] N. Smith, S. Kevan, and F. DiSalvo, Band structures of the layer compounds 1T-TaS₂ and 2H-TaSe₂ in the presence of commensurate charge-density waves, *J. Phys. Condens. Matter* **18**, 3175 (1985).
- [26] R. Kappera, D. Voiry, S. E. Yalcin, B. Branch, G. Gupta, A. D. Mohite, and M. Chhowalla, Phase-engineered low-resistance contacts for ultrathin MoS₂ transistors, *Nature Materials* **13**, 1128 (2014).
- [27] J. Xia, J. Wang, D. Chao, Z. Chen, Z. Liu, J.-L. Kuo, J. Yan, and Z. X. Shen, Phase evolution of lithium intercalation dynamics in 2H-MoS₂, *Nanoscale* **9**, 7533 (2017).
- [28] K.-A. N. Duerloo, Y. Li, and E. J. Reed, Structural phase transitions in two-dimensional Mo- and W-dichalcogenide monolayers, *Nature Communications* **5**, 4214 EP (2014).
- [29] A. Nourbakhsh, A. Zubair, R. N. Sajjad, A. Tavakkoli KG, W. Chen, S. Fang, X. Ling, J. Kong, M. S. Dresselhaus, E. Kaxiras, *et al.*, MoS₂ field-effect transistor with sub-10 nm channel length, *Nano Lett.* **16**, 7798 (2016).
- [30] F. Bischoff, W. Auwärter, J. V. Barth, A. Schiffrin, M. Fuhrer, and B. Weber, Nanoscale Phase Engineering of Niobium Diselenide, *Chem. Mater.* **29**, 9907 (2017).
- [31] F. J. Di Salvo, D. Moncton, and J. Waszczak, Electronic properties and superlattice formation in the semimetal TiSe₂, *Phys. Rev. B* **14**, 4321 (1976).
- [32] P. Chen, W. W. Pai, Y.-H. Chan, A. Takayama, C.-Z. Xu, A. Karn, S. Hasegawa, M.-Y. Chou, S.-K. Mo, A.-V. Fedorov, *et al.*, Emergence of charge density waves and a pseudogap in single-layer TiTe₂, *Nature Communications* **8**, 516 (2017).
- [33] C. Battaglia, H. Cercellier, F. Clerc, L. Despont, M. G. Garnier, C. Koitzsch, P. Aebi, H. Berger, L. Forró, and

- C. Ambrosch-Draxl, Fermi-surface-induced lattice distortion in NbTe₂, *Phys. Rev. B* **72**, 195114 (2005).
- [34] J. Wilson, F. Di Salvo, and S. Mahajan, Charge-density waves and superlattices in the metallic layered transition metal dichalcogenides, *Advances in Physics* **24**, 117 (1975) reprinted as Charge-density waves and superlattices in the metallic layered transition metal dichalcogenides, *Advances in Physics* **50**, 1171 (2001).
- [35] J. Wilson, F. Di Salvo, and S. Mahajan, Charge-density waves in metallic, layered, transition-metal dichalcogenides, *Phys. Rev. Lett.* **32**, 882 (1974).
- [36] J. Feng, A. Tan, S. Wagner, J. Liu, Z. Mao, X. Ke, and P. Zhang, Charge modulation and structural transformation in TaTe₂ studied by scanning tunneling microscopy/spectroscopy, *Applied Physics Lett.* **109**, 021901 (2016).
- [37] S. J. McDonnell and R. M. Wallace, Atomically-thin layered films for device applications based upon 2D TMDC materials, *Thin Solid Films* **616**, 482 (2016).
- [38] S. Manzeli, D. Ovchinnikov, D. Pasquier, O. V. Yazyev, and A. Kis, 2D transition metal dichalcogenides, *Nature Reviews Materials* **2**, 17033 (2017).
- [39] D. Voiry, A. Mohite, and M. Chhowalla, Phase engineering of transition metal dichalcogenides, *Chem. Soc. Rev.* **44**, 2702 (2017).
- [40] H. Cercellier, C. Monney, F. Clerc, C. Battaglia, L. Despont, M. Garnier, H. Beck, P. Aebi, L. Patthey, H. Berger, *et al.*, Evidence for an excitonic insulator phase in 1T-TiSe₂, *Phys. Rev. Lett.* **99**, 146403 (2007).
- [41] E. Morosan, H. W. Zandbergen, B. Dennis, J. Bos, Y. Onose, T. Klimczuk, A. Ramirez, N. Ong, and R. J. Cava, Superconductivity in Cu_xTiSe₂, *Nature Physics* **2**, 544 (2006).
- [42] L. Li, E. O'Farrell, K. Loh, G. Eda, B. Özyilmaz, and A. C. Neto, Controlling many-body states by the electric-field effect in a two-dimensional material, *Nature* **529**, 185 (2016).
- [43] M. Hellgren, J. Baima, R. Bianco, M. Calandra, F. Mauri, and L. Wirtz, Critical role of the exchange interaction for the electronic structure and charge-density-wave formation in TiSe₂, *Phys. Rev. Lett.* **119**, 176401 (2017).
- [44] C. Fang, R. De Groot, and C. Haas, Bulk and surface electronic structure of 1T-TiS₂ and 1T-TiSe₂, *Phys. Rev. B* **56**, 4455 (1997).
- [45] P. Chen, Y.-H. Chan, X.-Y. Fang, S.-K. Mo, Z. Hussain, A.-V. Fedorov, M. Chou, and T.-C. Chiang, Hidden order and dimensional crossover of the charge density waves in TiSe₂, *Scientific reports* **6**, 37910 (2016).
- [46] C. Xu, P. A. Brown, and K. L. Shuford, Strain-induced semimetal-to-semiconductor transition and indirect-to-direct band gap transition in monolayer 1T-TiS₂, *RSC Advances* **5**, 83876 (2015).
- [47] C. J. Carmalt, T. D. Manning, I. P. Parkin, E. S. Peters, and A. L. Hector, Formation of a new (1t) trigonal NbS₂ polytype via atmospheric pressure chemical vapour deposition, *Journal of Materials Chemistry* **14**, 290 (2004).
- [48] M. Van Maaren and G. Schaeffer, Some new superconducting group V^a dichalcogenides, *Physics Letters A* **24**, 645 (1967).
- [49] L. Li, W. Lu, X. Zhu, L. Ling, Z. Qu, and Y. Sun, Fedoping-induced superconductivity in the charge-density-wave system 1T-TaS₂, *EPL* **97**, 67005 (2012).
- [50] Y. Liu, R. Ang, W. Lu, W. Song, L. Li, and Y. Sun, Superconductivity induced by Se-doping in layered charge-density-wave system 1T-TaS_{2-x}Se_x, *Appl. Phys. Lett.* **102**, 192602 (2013).
- [51] Y. Liu, D. Shao, L. Li, W. Lu, X. Zhu, P. Tong, R. Xiao, L. Ling, C. Xi, L. Pi, *et al.*, Nature of charge density waves and superconductivity in 1T-TaSe_{2-x}Te_x, *Phys. Rev. B* **94**, 045131 (2016).
- [52] G. Kresse and J. Furthmüller, Efficient iterative schemes for ab initio total-energy calculations using a plane-wave basis set, *Phys. Rev. B* **54**, 11169 (1996).
- [53] G. Kresse and J. Furthmüller, Efficiency of ab-initio total energy calculations for metals and semiconductors using a plane-wave basis set, *Computational materials science* **6**, 15 (1996).
- [54] J. P. Perdew, K. Burke, and M. Ernzerhof, Generalized gradient approximation made simple, *Phys. Rev. Lett.* **77**, 3865 (1996).
- [55] S. Grimme, J. Antony, S. Ehrlich, and H. Krieg, A consistent and accurate ab initio parametrization of density functional dispersion correction (DFT-D) for the 94 elements H-Pu, *The Journal of chemical physics* **132**, 154104 (2010).
- [56] A. A. Mostofi, J. R. Yates, Y.-S. Lee, I. Souza, D. Vanderbilt, and N. Marzari, wannier90: A tool for obtaining maximally-localised Wannier functions, *Computer physics communications* **178**, 685 (2008).
- [57] N. Marzari and D. Vanderbilt, Maximally localized generalized Wannier functions for composite energy bands, *Phys. Rev. B* **56**, 12847 (1997).
- [58] I. Souza, N. Marzari, and D. Vanderbilt, Maximally localized Wannier functions for entangled energy bands, *Phys. Rev. B* **65**, 035109 (2001).
- [59] H. Li, A. W. Contryman, X. Qian, S. M. Ardakani, Y. Gong, X. Wang, J. M. Weisse, C. H. Lee, J. Zhao, P. M. Ajayan, *et al.*, Optoelectronic crystal of artificial atoms in strain-textured molybdenum disulphide, *Nature Communications* **6**, 7381 (2015).
- [60] R. Banerjee, V.-H. Nguyen, T. Granzier-Nakajima, L. Pabbi, A. Lherbier, A. Binion, J.-C. Charlier, M. Terrones, and E. Hudson, Strain modulated superlattices in graphene, *arXiv:1903.10468 [cond-mat.mes-hall]* (2019).
- [61] T. B. Boykin and G. Klimeck, Practical application of zone-folding concepts in tight-binding calculations, *Phys. Rev. B* **71**, 115215 (2005).
- [62] W. Ku, T. Berlijn, C.-C. Lee, *et al.*, Unfolding first-principles band structures, *Phys. Rev. Lett.* **104**, 216401 (2010).
- [63] V. Popescu and A. Zunger, Extracting *E* versus *k* effective band structure from supercell calculations on alloys and impurities, *Phys. Rev. B* **85**, 085201 (2012).
- [64] O. Rubel, A. Bokhanchuk, S. J. Ahmed, and E. Assmann, Unfolding the band structure of disordered solids: From bound states to high-mobility Kane fermions, *Phys. Rev. B* **90**, 115202 (2014).
- [65] J. Cao, V. Fatemi, A. Demir, S. Fang, S. L. Tomarken, J. Y. Luo, J. D. Sanchez-Yamagishi, K. Watanabe, T. Taniguchi, E. Kaxiras, R. C. Ashoori, and P. Jarillo-Herrero, Correlated insulator behaviour at half-filling in magic-angle graphene superlattices, *Nature* **556**, 80 EP (2018).
- [66] Y. Cao, V. Fatemi, S. Fang, K. Watanabe, T. Taniguchi, E. Kaxiras, and P. Jarillo-Herrero, Unconventional superconductivity in magic-angle graphene superlattices, *Nature*

- ture **556**, 43 EP (2018).
- [67] M. Yankowitz, S. Chen, H. Polshyn, Y. Zhang, K. Watanabe, T. Taniguchi, D. Graf, A. F. Young, and C. R. Dean, Tuning superconductivity in twisted bilayer graphene, *Science* 10.1126/science.aav1910 (2019).
 - [68] N. N. T. Nam and M. Koshino, Lattice relaxation and energy band modulation in twisted bilayer graphene, *Phys. Rev. B* **96**, 075311 (2017).
 - [69] J. Jung, A. Raoux, Z. Qiao, and A. H. MacDonald, Ab initio theory of moiré superlattice bands in layered two-dimensional materials, *Phys. Rev. B* **89**, 205414 (2014).
 - [70] S. Fang and E. Kaxiras, Electronic structure theory of weakly interacting bilayers, *Phys. Rev. B* **93**, 235153 (2016).